frontiers | Frontiers in Earth Science

ORIGINAL RESEARCH
published: 03 June 2022
doi: 10.3389/feart.2022.910453

Effects of Deep Fluids on Middle Permian Dolomite of the Western Sichuan Basin

Huiwen Huang[1,2], *Hongde Chen*[1,2], *Fei Huo*[1,2]*, *Shuai Yang*[1,2] *and Anqing Chen*[1,2]*

[1]*Institute of Sedimentary Geology, Chengdu University of Technology, Chengdu, China,* [2]*State Key Laboratory of Oil and Gas Reservoir Geology and Exploitation, Chengdu University of Technology, Chengdu, China*

Deep fluid activity is closely related to carbonate reservoir transformation as well as oil and gas accumulation. The large-scale deep fluid activity caused by Emeishan large igneous province (ELIP) brought a lot of deep material and energy to Sichuan Basin and changed the paleogeothermal and geochemical field of the region they flowed through, which had an important impact on the formation of the Middle Permian dolomite reservoir in Western Sichuan. Through comprehensive analyses of petrographic, geochemical, and fluid inclusion data from two drill cores and three outcrop sections of the Middle Permian Formation in the Western Sichuan Basin, the dolomitizing fluid, dolomite genesis, and effect of deep fluid were discussed. The dolomite was divided into four types which are matrix dolomites (Md1, Md2, and Md3) and cement dolomites (Cd). Among them, the Md1 was formed in penecontemporaneous seawater by seepage reflux dolomitization, while Md2 was formed in heated Permian seawater through thermal convection. In the northwest of the study area, the Md3 and Cd were formed by higher-temperature thermal convection without hydrothermal. In the southwest of the study area, the lower $\delta^{13}C$ value and Sr contents, higher Mn contents and $^{87}Sr/^{86}Sr$ ratios, and positive Eu anomalies as well as much higher T_h and salinity values of inclusions show that hydrothermal participated in the dolomitization, forming the Md3 and Cd through structure-hydrothermal dolomitization and the thermal convection of seawater mixed with hydrothermal. The deep fluid activities of ELIP provided both the material source (Mg^{2+}) for the dolomitization process and the migration motive power for the dolomitization fluid. From the southwest to northwest, with the deep fluid activity decreasing, the abundance of Md3 and Cd, which are closely related to the hydrothermal solution, reduced.

Keywords: deep fluids, hydrocarbon accumulations, dolomite reservoirs, Sichuan Basin, dolomitization

OPEN ACCESS

Edited by:
Chen Zhang,
Chengdu University of Technology, China

Reviewed by:
Cuiting Qi,
Texas A&M University, United States
Kelai Xi,
China University of Petroleum, China

***Correspondence:**
Fei Huo
huofei342099206@163.com
Anqing Chen
chenanqing2012@cdut.edu.cn

Specialty section:
This article was submitted to Structural Geology and Tectonics, a section of the journal Frontiers in Earth Science

Received: *01 April 2022*
Accepted: *19 April 2022*
Published: *03 June 2022*

Citation:
Huang H, Chen H, Huo F, Yang S and Chen A (2022) Effects of Deep Fluids on Middle Permian Dolomite of the Western Sichuan Basin. Front. Earth Sci. 10:910453. doi: 10.3389/feart.2022.910453

1 INTRODUCTION

In recent years, the significance of oil and gas accumulation of deep fluid is an important research topic in the field of oil and gas geology. Large-scale deep fluid activities bring a large amount of deep material and energy to the basin, change the paleogeothermal field and geochemical field of the region they flow through, and significantly change the composition and properties of sedimentary rocks directly (such as contact metamorphism) or indirectly (such as regional magmatic heating and compression fracture) and then further affect all stages of oil and gas formation and evolution in the

basin (Liu et al., 2010; Zhang et al., 2021). Deep fluids mostly refer to all fluids from below the basement of sedimentary basins (Jin et al., 2002; Liu et al., 2005; Hu, 2016), including deep rigid crustal- and mantle-derived fluids. Some scholars also classify hydrocarbon source thermal fluids related to hydrocarbon generation under deep burial conditions as deep fluids (Dai et al., 1995). Crust-derived fluids often come from deep ancient strata and crystalline basement and are often related to volcanic magmatic events (Hu, 2016). Mantle fluid is dominated by the C-H-O-S system, with alkaline elements, rare gases, and a small amount of trace components (Zhang et al., 2000). Deep source thermal fluid has obvious distinguishing signs in terms of rock mineralogy, fluid inclusions, and geochemical anomalies (Hu, 2016). In addition, heavy metal elements, magmatism, deep structure, and paleogeothermal anomalies (Zeng, 2000; Jin et al., 2002) can be used as evidence of deep fluid transformation or activity.

In Southwest China, Emeishan large igneous province (ELIP) is the first recognized large igneous province in China by international academic circles (Xu et al., 2004, 2008; Sun et al., 2010). The deep fluid activity brought by large-scale basalt eruption made the deep material and energy migrate to the surface, affected the shallow surface system, magmatic and hydrothermal metallogenic system (Du et al., 2020), and controlled the sedimentary characteristics and lithofacies paleogeographic environment of its influence range (He et al., 2003; Xu et al., 2004; Song et al., 2008). Among them, the Middle Permian dolomite reservoir in Sichuan Basin, as a high-yield horizon that plays an important role in natural gas exploration in Sichuan Basin, is particularly affected by the deep fluid related to ELIP. The explaining models of dolomitization of Middle Permian dolomite are varied, such as mixed water (Badiozamani, 1973; Zhang et al., 2018), basalt leaching (Jin and Feng, 1999), seepage reflux (Adams and Rhodes, 1960), burial (Mattes and Mountjoy, 1980; Jiang et al., 2009), hydrothermal (Jiang et al., 2014; Xia et al., 2020), and thermal convection (Simms, 1984; Machel, 2004), and superposition of multistage (Tian et al., 2014). Among them, the hydrothermal dolomitization related to the ELIP is generally accepted (Huang et al., 2011; Chen et al., 2013; Ramkumar et al., 2019; Zheng et al., 2019).

While the hydrothermal dolomitization may be persuasive in explaining the genesis of dolomite near ELIP and fault zones, the dolomites in distal zones may not be convincing as the latter lack typical hydrothermal features in geochemistry and petrology, such as high homogenization temperatures (T_h) and typical hydrothermal minerals like fluorites and siderites (Chen et al., 2013; Zheng et al., 2019), providing evidence for nonhydrothermal dolomitization which may be drawn as thermal convection (Dong et al., 2020). Thus, it can be seen that the material and energy brought by deep fluid activities change with distance and accordingly have different effects on the formation of dolomite under different mechanisms.

Previous studies mainly focused on the influence of sedimentation, structure, and diagenesis on dolomitization, while less on deep fluid. Through petrological, fluid inclusion, and geochemical analysis, we studied the dolomitization fluid types, thermal conditions, and formation mechanism of the Middle Permian dolomite reservoir in the Western Sichuan Basin. We expounded on the influence of the changes of paleogeothermal and paleochemical fields caused by the deep fluid activity related to the Emeishan large igneous province (ELIP) on dolomitization, which provided an important reference significance for further understanding the role of deep fluid activity in the reconstruction of carbonate reservoirs in sedimentary basins.

2 GEOLOGICAL SETTING

The Sichuan Basin, a composite superimposed craton basin with multiple tectonic cycles, is part of the Upper Yangtze Block of southern China (**Figure 1A**), located at low latitudes near the equator on the eastern side of the Paleo-Tethys Ocean in the Permian (Scotese and Schettino, 2017). It is bound by the Emeishan–Liangshan fold belt in the southwest, the Longmenshan fold belt in the northwest, and the Songpan-Ganzi, Qinling, and Dabashan fold belts in the north (Mei et al., 2014; Mei et al., 2016; Zheng et al., 2019). The study region is located in the Western Sichuan Basin, spans the regions of Emei, Yaan, Leshan, Jiangyou, Guangyuan, and Wangcang (**Figure 1B**).

The Middle Permian in the Sichuan Basin consists of the Qixia Formation and the Maokou Formation, which conformably overlies the Liangshan Formation and unconformably underlies the Wujiaping (Longtan) Formation. The sedimentary facies of Middle Permian in Western Sichuan are generally shallow-water carbonate platforms with normal to high salinity and abundant marine organisms (**Figure 1C**) (Wei et al., 2010; Zhou et al., 2016). After the long hiatus from the Late Carboniferous to Early Permian, there occurred a large-scale transgression in the Upper Yangtze region during the Kungurian, followed by a steady sea level decrease, and there was a transition from the coal-bearing clastic shore facies of the Liangshan Formation to carbonate platform facies of the Qixia Formation (Zhao et al., 2012). Subsequently, in the late Kungurian, the decrease in the sea level became steady. The rifting and extension was the dominant tectonic movement during this period due to the subduction of the Paleo-Tethys oceanic crusting toward the Yangtze plate (Zhao et al., 2012; Xiao et al., 2018; Zhu et al., 2019). The Qixia Formation mainly consists of gray dolomite, dark-gray thin-bedded limestone, and medium-to-thin-bedded bioclastic limestone. With the activity of Longmenshan fault, the west side of the Longmenshan fault resides on the lower terrain, deepening the water of the basin (**Figure 1C**) (Chen, 2009; Wei et al., 2010; Huang et al., 2017). During the early Guadalupian, large-scale and long-term transgression occurred (Hu et al., 2012; Saitoh et al., 2013). The Maokou Formation was in the deep-water depositional environment. Thus, the sediments of the Maokou Formation are mainly deposited as thick layers of dark-gray bioclastic

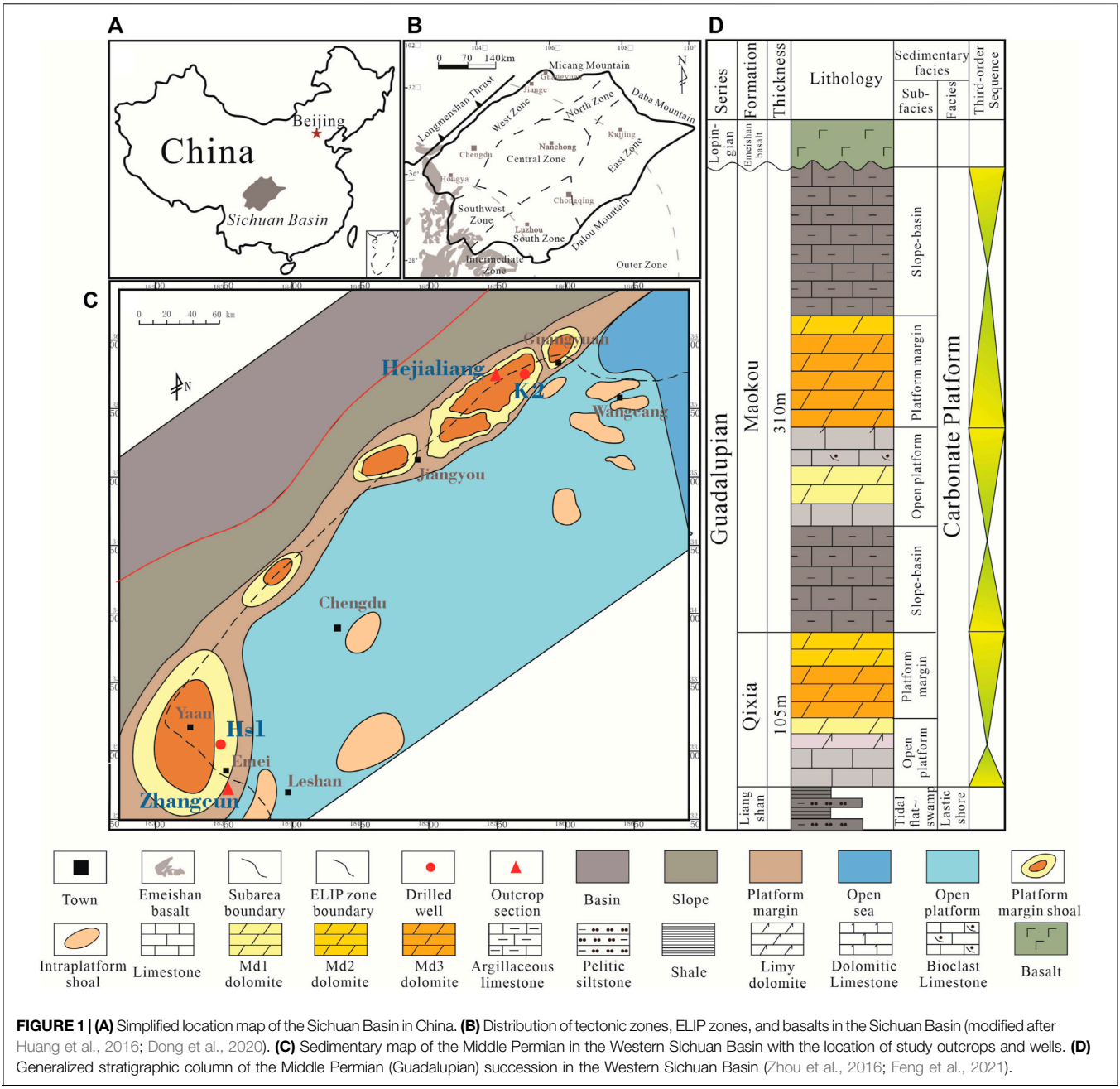

FIGURE 1 | (A) Simplified location map of the Sichuan Basin in China. **(B)** Distribution of tectonic zones, ELIP zones, and basalts in the Sichuan Basin (modified after Huang et al., 2016; Dong et al., 2020). **(C)** Sedimentary map of the Middle Permian in the Western Sichuan Basin with the location of study outcrops and wells. **(D)** Generalized stratigraphic column of the Middle Permian (Guadalupian) succession in the Western Sichuan Basin (Zhou et al., 2016; Feng et al., 2021).

limestone, black muddy limestone, shale, and a few gray dolomites (Chen et al., 2013) (**Figure 1D**).

The study area was buried rapidly after deposition according to the reconstructed burial history model of the Middle Permian strata of Well Hanshen1 (**Figure 2**) in the southwestern part of our study area. Then, there was a small structural uplift due to the Variscan orogeny (Dongwu Movement), with the erosion of varying degrees to the Maokou Formation owing to the uplift related to the magmatic upwelling before the eruption of the Emeishan basalt (He et al., 2003; Zheng et al., 2019). Subsequently, the Permian strata increasingly subsided during the Triassic. It was not until the latest Triassic that an uplift (without exposure and erosion) due to the Indosinian Movement appeared. Followed by the continuous increase in burial depth from Jurassic to Paleogene, the strata were not uplifted again until the Neogene because of the constant Himalayan Orogeny (Richardson et al., 2008).

From the end of the Guadalupian to the beginning of the Lopingian, the Variscan orogeny (Dongwu Movement) occurred. Emeishan basalts erupted on a large scale in pace with the activity of the Emeishan mantle plume, forming a large igneous province (Mahoney and Coffin, 1997; Courtillot et al., 1999). The general understanding of the eruption time is considered to be about 260 Ma lasting for less than 3 M.y. (He et al., 2007; Shellnutt et al.,

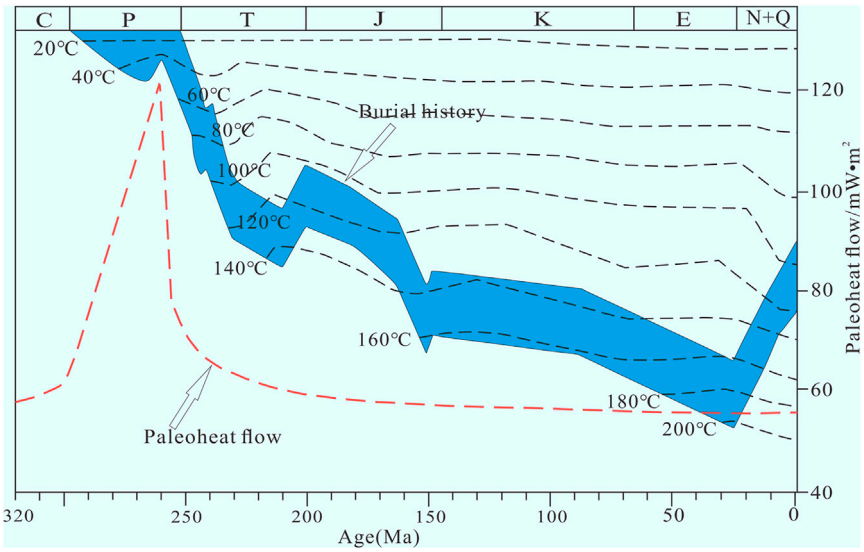

FIGURE 2 | Schematic map of burial history, paleotemperature, and paleoheat flow distribution of the Middle Permian (the blue part) in Well HS1 of the Western Sichuan Basin (Cai et al., 2004; Zhu et al., 2010; Wei et al., 2016; Zheng et al., 2019).

2012; Dong et al., 2020). Evidence confirmed that the Emeishan large igneous province (ELIP) caused faulting which raised the regional geothermal temperature. There experienced a heat flow which commenced at ca. 290 Ma. The heat flow increase gradually during the Permian period and peaked when the ELIP erupted at ca. 259 Ma. In the study area, the paleoheat flow was relatively high in the southwestern (50–120 mW/m^2) while relatively low in the northwestern (50–75 mW/m^2) (Zhu et al., 2010; Dong et al., 2020).

3 SAMPLES AND METHODS

In this study, a total of 7 samples of the Xinjigu (XJG) section, 11 samples of the Zhangcun (ZC) section, 5 samples from the drill cores of Well HS1, 18 samples of the Hejialiang (HJL) section, and 7 samples from the drill cores of Well K2 in Western Sichuan Basin were collected for geochemical and fluid inclusion analyses. The lithologies of the samples are dominated by dolomite (41 samples) and limestone (7 samples) (**Figure 3**; **Tables 1**–**4**). We attempted to select samples without impurities, and thus the samples were taken from fresh sections of drilling cores by micro-drilling; all samples were identified under a microscope (including alizarin red and potassium ferricyanide staining and casting slice analysis). At the same time, the samples used for geochemical analysis were carefully sorted under binoculars to avoid calcite veins and bright calcite cement as far as possible to ensure the reliability of the classified samples. The samples were ground in an agate mortar at a slow speed and pulverized into a 200-mesh sieve (<75 μm).

The C, O isotopic assays were processed and analyzed at the Key Laboratory of Orogenic Belts and Crustal Evolution, Peking University, China. Samples were measured using the IsoPrime 100 instrument after 16 h of soaking in 99% phosphoric acid at 70–80°C with an analytical accuracy of ±0.1‰. All results were conducted under the Vienna Peedee Belemnite standard (VPDB). Sr isotopes were also analyzed in the same place. The samples were dissolved in HCl, and measurement was performed using a Triton™ mass spectrometer with a standard deviation of $\pm 1.0 \times 10^{-5}$.

Trace elements and rare Earth elements (REEs) analyses were implemented at the Sichuan Metallurgical Geological Rock and Mineral Testing Center, China, using the ICP-MS, with an analytical precision of ±5‰. Mn and Sr were tested by atomic absorption spectrophotometry, of which the detection limits were 5 and 42 ppm, respectively, and the errors were 13% and 14%, respectively. The measured REE concentrations were normalized to the Post-Archean Australian Shale composite (PAAS) (Pourmand et al., 2012), with results marked by the subscript, $_{SN,}$ after normalization.

Owing to the general anomaly of La in marine carbonate rocks, it was inappropriate to use $\delta Ce = Ce/Ce^* = Ce_{SN}/(0.5La_{SN} + 0.5Pr_{SN})$ to calculate the Ce anomaly (Bau and Dulski, 1996; Zhou et al., 2008; Liu et al., 2017). It was more accurate to use $\delta Ce = Ce/Ce^* = Ce_{SN}/(Pr^2_{SN}/Nd_{SN})$ instead. Since there was a lack of the abnormally enriched Gd, the formula $Eu/Eu^* = Eu_{SN}/(0.5Sm_{SN} + 0.5Tb_{SN})$ was used to calculate the Eu anomalies (Bau and Dulski, 1996). The $(Nd/Yb)_{SN}$ ratio was used to reflect the relative enrichment of light REE (LREE) and heavy REE (HREE) in fractionation.

Fluid inclusion microthermometry was conducted at the Microscopic Hydrocarbon Detection Laboratory of China University of Geosciences (Wuhan). The homogenization temperatures (T_h) and final melting temperatures (T_m) were measured by a Linkam THMGS600 heating-freezing stage for two-phase aqueous inclusions. The accuracy of T_h and T_m are ±1°C and ±0.1°C, respectively. Salinities were

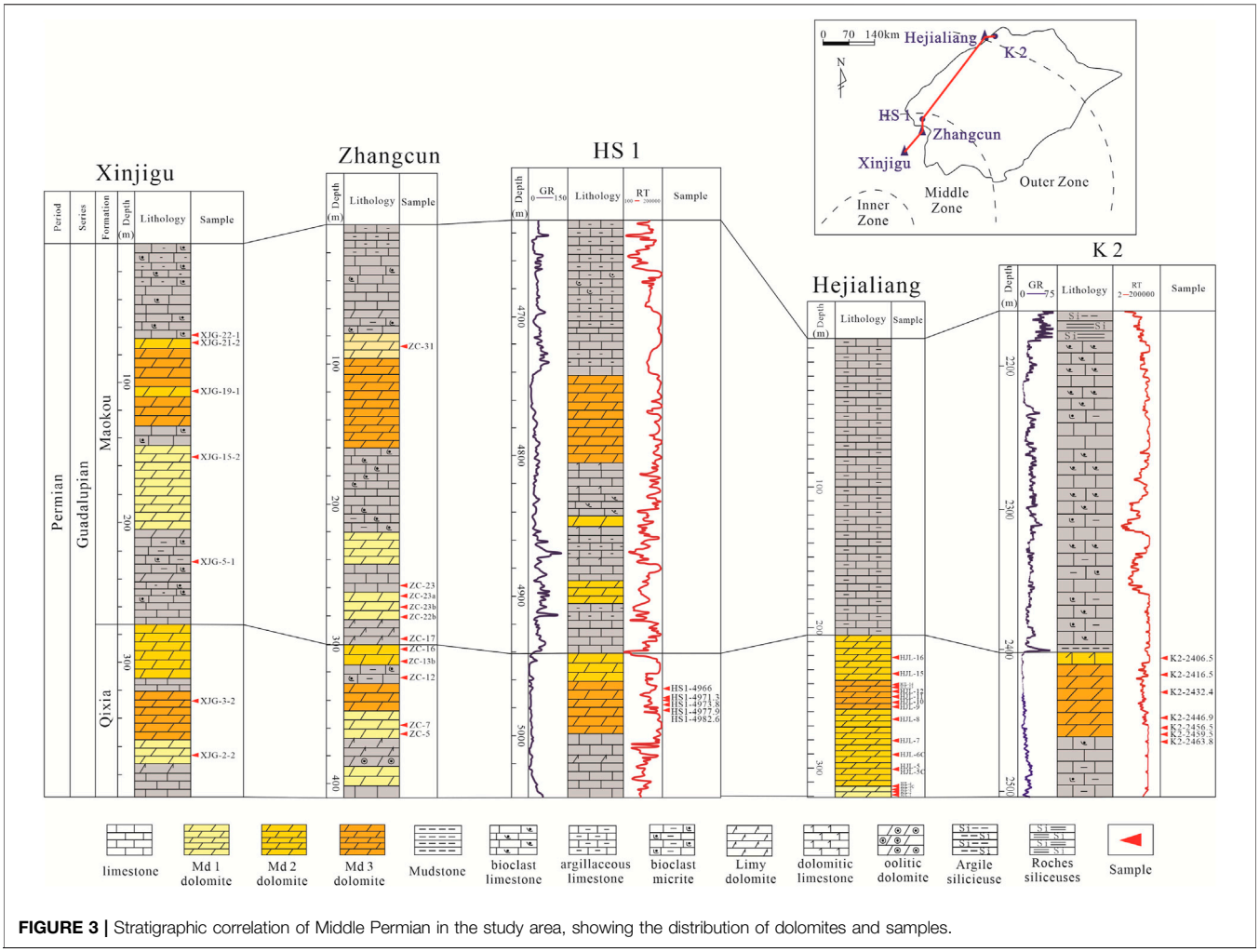

FIGURE 3 | Stratigraphic correlation of Middle Permian in the study area, showing the distribution of dolomites and samples.

calculated by T_m using the formula according to Steele–MacInnis et al. (2011).

4 RESULTS

4.1 Petrological Characteristics

The carbonate rocks in the Western Sichuan Basin were mainly composed of limestones, dolomites, and transitional rocks such as dolomitic limestones and limy dolomites. The dolomite samples of the study area can be divided into matrix dolomite (Md) and cement dolomite (Cd, dominated by saddle dolomite), of which the Md samples can be further divided into three types, which are Md1 with very finely to finely crystalline, Md2 with medium to finely crystalline and Md3 with coarsely to medium crystalline (Bissell and Chilingar, 1967; Dong et al., 2020). The characteristics of these four types of dolomites mentioned previously are described as follows:

(1) Md1 usually appears gray–dark-gray in the hand specimen. It has a very finely to finely crystalline size (<0.25 mm) and is mostly xenomorphic with indistinct crystal rims with relatively dense and low porosity (**Figure 4A**). It partly preserves sedimentary fabrics from the precursor limestones and occasionally develops terrestrial quartz grains. Generally, Md1 is found at the bottom of the Qixia Formation and the middle-bottom of the Maokou Formation.

(2) Md2 consists of planar-e to planar-s dolomite crystals with unhomogeneous sizes of 50–450 μm. The crystals are commonly with cloudy-core and clear-rim textures (**Figure 4B**). It preserves no original fabrics and merely retains a few ghost outlines of the precursor particles. There exist abundant intercrystalline pores filled with bitumen (**Figure 4C**). It presents special dark patches associated with light limestone as partially dolomitized at the top of the Qixia Formation mostly in the northwestern Sichuan Basin, while completely dolomitized in the other parts.

(3) The Md3 appears brown-gray in the hand specimen. It consists of larger and more homogeneous crystals (350–800 μm), which are generally nonplanar-a and few planar-s. It differs from the Md2 as the crystals of Md3 are turbid without clear rims, showing sharp undulatory

TABLE 1 | Stable isotope data for Middle Permian carbonates of the Western Sichuan Basin.

Region	Sample	Lithology	$\delta^{13}C$ (‰V_{PDB})	$\delta^{18}O$ (‰V_{PDB})	$^{87}Sr/^{86}Sr$
NW	K2-2456.5	Limestone	2.6	−6.1	fx130.70707
	K2-2459.5		2.6	−6.2	0.70771
	K2-2463.8		3.6	−3.9	0.70727
	HJL- 1	Md1	2.4	−4	0.70737
	HJL-2		2.7	−6.3	0.70762
	HJL-3		2.5	−5.7	0.70785
	HJL-4		1.5	−5.7	0.70769
	K2-2406.3	Md2	3.5	−4.3	0.70727
	K2-2416.3		3	−4.8	0.70742
	K2-2432.4		2.2	−6.6	—
	K2-2446.9		3	−5.5	0.70752
	HJL-5		1	−5.4	—
	HJL-7		1.2	−6.3	0.70769
	HJL-8		1.2	−6	0.70753
	HJL- 15		1.6	−6.3	0.70758
	HJL-16		1.3	−5.1	—
	HJL-9	Md3	2.2	−7	0.70745
	HJL-10		2	−6.8	0.7076
	HJL-11		2.5	−6.9	0.7074
	HJL-12		3	−7.1	—
	HJL-13		2.7	−6.5	0.70738
	HJL-14		2	−7.4	—
NW	HJL-4C	Cd	2.3	−6.9	0.70764
	HJL-5C		2.9	−7.4	0.70769
	HJL-6C		2.9	−6.9	0.70779
SW	ZC-12	Limestone	4.6	−8.4	0.70753
	ZC-23		4.5	−7.7	0.70682
	XJG-5-1		3.4	−7.4	0.70709
	ZC-5	Md1	4.2	−8.6	0.70732
	ZC-7		4.3	−5.9	0.70754
	XJG-15-2		3.8	−5.2	0.70774
	XJQ-2-2	Md2	3.6	−7.1	0.70801
	XJG-21-2		3.8	−5.5	0.70768
	XJQ-3-2		3.4	−8.7	0.70786
	XJG-19-1		4.09	−6.65	0.70709
	ZC-16		4.2	−10.74	0.70754
	ZC-31		4.7	−5.2	0.70734
	HS1 4966	Md3	3.6	−11	0.71065
	HS1 4971.3		3.4	−11.3	0.70981
	ZC-23a		3.7	−11.2	0.70870
	ZC-17		3.3	−11.6	—
	ZC-13b	Cd	2.1	−11.7	—
	ZC-22b		3.2	−11.4	0.71018
	ZC-23b		3.4	−11.6	0.70958

extinction under cross-polarized light (**Figure 4G**). Moreover, the Md3 is abundant in dissolution pores and fractures, which are partly infilled with bitumen or cement of quartz, dolomite, and calcite (**Figures 4E, F, H**). What is similar to Md2 is that their fabric structure is destroyed, which led the initial fabric and/or early diagenetic features which are hard to be remained.

(4) Cd is filled along the dissolution pores and fractures appearing white-gray–white. The crystal size is larger than that of Md (>400 μm). The crystals are nonplanar-a to saddle textures showing undulatory extinction under cross-polarized light (**Figures 4C, D, I**). The abundance of Cd is relatively lower in the northwestern Sichuan Basin compared to the southwestern Sichuan Basin (Liu et al., 2017; Zheng et al., 2019).

4.2 Geochemical Characteristics

4.2.1 Stable Carbon and Oxygen Isotope Characteristics

In the northwestern Sichuan Basin, the $\delta^{13}C$ values of the limestone range from 2.6‰ to 3.6‰ (avg. 2.9‰) and the $\delta^{18}O$ values from −6.2‰ to −3.9‰ (avg. −5.4‰). The $\delta^{13}C$ values of Md1 span from 1.5‰ to 2.7‰ (avg. 2.3‰) and $\delta^{18}O$ values from −6.3‰ to −4.0‰ (avg. −5.4‰). For Md2, $\delta^{13}C$ values are in the range of 1.0–3.5‰ (avg. 2.0‰) and the $\delta^{18}O$ values are in the range of −6.6‰ to −4.3‰ (avg.−5.6‰). Obviously, the $\delta^{13}C$ and $\delta^{18}O$ values of both Md1 and Md2 overlap those of limestone as well as the $\delta^{13}C$ (3.1‰–5.5‰) and $\delta^{18}O$ values (−4.3‰–0.1‰) of calcites precipitated from Permian seawater (Korte et al., 2005; Mii et al., 2012; Buggisch et al., 2015). As for Md3, $\delta^{13}C$ values are in the range of 2.0–3.0‰ (avg. 2.4‰) and

TABLE 2 | Major and trace elements data for Middle Permian carbonates of the northwestern (NW) study area (10^{-6} mg/g).

Sample	Lithology	La	Ce	Pr	Nd	Sm	Eu	Gd	Tb	Dy	Ho	Er	Tm	Yb	Lu	Y	Y/Ho	ΣREE	Ce/Ce*	Eu/Eu*	Sr	Mn	Mn/Sr	$(Nd/Yb)_{SN}$
K2-2456.5	Limestone	2.10	4.07	0.46	1.84	0.46	0.09	0.49	0.07	0.41	0.08	0.21	0.03	0.17	0.02	3.42	42.81	10.49	0.90	0.82	307	38	0.12	0.95
K2-2459.5		0.70	1.42	0.17	0.63	0.15	0.02	0.12	0.02	0.11	0.02	0.06	0.01	0.07	0.01	1.22	61.09	3.51	0.80	0.69	289	11	0.04	0.79
K2-2463.8		0.41	0.78	0.10	0.34	0.08	0.01	0.07	0.01	0.06	0.01	0.03	0.01	0.03	0.00	0.62	62.18	1.95	0.76	0.76	313	37	0.12	0.99
HJL-1	Md1	2.07	3.99	0.46	1.73	0.47	0.09	0.50	0.08	0.47	0.09	0.24	0.03	0.21	0.03	5.32	59.07	10.46	0.85	0.78	83	56	0.67	0.72
HJL-2		3.29	6.12	0.71	2.58	0.63	0.12	0.64	0.09	0.55	0.10	0.25	0.04	0.23	0.03	4.47	44.65	15.38	0.82	0.80	78	60	0.77	0.98
HJL-3		2.97	5.62	0.65	2.39	0.60	0.11	0.61	0.09	0.54	0.10	0.25	0.03	0.22	0.03	5.61	56.09	14.23	0.82	0.80	76	62	0.82	0.95
HJL-4		0.83	1.59	0.18	0.71	0.17	0.03	0.17	0.03	0.16	0.03	0.09	0.01	0.08	0.01	2.01	66.94	4.10	0.91	0.84	105	49	0.47	0.78
K2-2406.3	Md2	0.44	0.83	0.10	0.37	0.10	0.02	0.10	0.01	0.09	0.02	0.05	0.01	0.05	0.01	1.41	70.28	2.20	0.82	0.87	86	74	0.86	0.65
K2-2416.3		0.46	0.87	0.11	0.40	0.09	0.02	0.09	0.01	0.08	0.02	0.04	0.01	0.05	0.01	1.39	69.34	2.25	0.80	0.82	96	43	0.45	0.70
K2-2432.4		0.33	0.64	0.07	0.27	0.06	0.01	0.05	0.01	0.04	0.01	0.02	0.00	0.02	0.00	0.66	65.89	1.56	0.81	0.72	117	52	0.44	1.18
K2-2446.9		0.40	0.80	0.09	0.35	0.08	0.01	0.07	0.01	0.06	0.01	0.03	0.00	0.03	0.00	0.68	67.63	1.94	0.87	0.86	84	80	0.95	1.02
HJL-5		1.02	1.95	0.23	0.86	0.21	0.03	0.18	0.03	0.16	0.03	0.09	0.01	0.10	0.02	2.07	68.98	4.92	0.85	0.77	85	57	0.67	0.75
HJL-7		0.56	1.07	0.12	0.48	0.11	0.02	0.10	0.01	0.08	0.02	0.05	0.01	0.05	0.01	1.26	63.19	2.69	0.87	0.80	65	59	0.91	0.84
HJL-8		0.53	1.02	0.11	0.44	0.10	0.02	0.10	0.01	0.08	0.02	0.04	0.01	0.04	0.01	1.33	66.35	2.52	0.89	0.79	74	46	0.62	0.96
HJL-15		0.62	1.14	0.13	0.49	0.11	0.02	0.10	0.02	0.10	0.02	0.05	0.01	0.06	0.01	1.41	70.74	2.86	0.92	0.82	74	59	0.80	0.71
HJL-16		0.84	1.60	0.18	0.68	0.15	0.02	0.13	0.02	0.12	0.02	0.06	0.01	0.07	0.01	1.39	69.73	3.92	0.82	0.73	87	59	0.68	0.85
HJL-9	Md3	0.47	0.86	0.10	0.40	0.09	0.02	0.08	0.01	0.08	0.02	0.05	0.01	0.04	0.01	1.33	66.39	2.25	0.84	0.90	51	72	1.41	0.88
HJL-10		0.46	0.86	0.10	0.37	0.09	0.02	0.08	0.01	0.08	0.02	0.05	0.01	0.04	0.01	1.35	67.37	2.18	0.83	0.90	40	66	1.65	0.81
HJL-11		0.46	0.84	0.10	0.37	0.09	0.02	0.09	0.01	0.08	0.02	0.05	0.01	0.04	0.01	1.44	71.84	2.17	0.84	0.88	52	75	1.44	0.81
HJL-12		0.49	1.02	0.12	0.47	0.11	0.02	0.10	0.02	0.09	0.02	0.04	0.01	0.04	0.01	1.40	70.23	2.56	0.84	0.89	66	58	0.88	1.03
HJL-13		0.61	1.11	0.12	0.49	0.12	0.02	0.11	0.02	0.10	0.02	0.05	0.01	0.05	0.01	1.29	64.74	2.84	0.92	0.93	57	70	1.23	0.86
HJL-14		0.44	0.80	0.10	0.38	0.09	0.02	0.09	0.01	0.09	0.02	0.05	0.01	0.04	0.01	1.49	74.38	2.14	0.86	1.00	50	56	1.12	0.83
HJL-4C	Cd	0.31	0.58	0.06	0.24	0.05	0.01	0.04	0.01	0.04	0.01	0.03	0.00	0.02	0.00	0.79	78.64	1.41	0.95	0.97	52	51	0.98	1.05
HJL-5C		0.31	0.66	0.08	0.27	0.06	0.01	0.05	0.01	0.05	0.01	0.03	0.00	0.02	0.00	0.72	71.62	1.56	0.77	0.93	86	48	0.56	1.18
HJL-6C		0.47	0.85	0.09	0.34	0.08	0.02	0.08	0.01	0.07	0.01	0.04	0.01	0.04	0.01	0.70	69.81	2.10	0.90	0.97	74	58	0.78	0.74

TABLE 3 | Major and trace elements data for Middle Permian carbonates of the southwestern (SW) study area (10^{-6} mg/g).

Sample	Lithology	La	Ce	Pr	Nd	Sm	Eu	Gd	Tb	Dy	Ho	Er	Tm	Yb	Lu	Y	Y/Ho	ΣREE	Ce/Ce*	Eu/Eu*	Sr	Mn	Mn/Sr	$(Nd/Yb)_{SN}$
XJG-22-1	Limestone	0.64	1.46	0.18	0.66	0.14	0.02	0.12	0.02	0.10	0.02	0.05	0.01	0.05	0.01	0.94	47.21	3.49	0.80	0.79	730	50	0.07	1.16
ZC-12		3.40	7.77	0.88	3.44	0.75	0.08	0.57	0.08	0.41	0.07	0.17	0.03	0.17	0.02	3.16	45.18	17.86	0.90	0.57	640	30	0.05	1.77
ZC-23		1.43	2.77	0.30	1.15	0.24	0.04	0.21	0.03	0.19	0.04	0.11	0.02	0.12	0.02	2.09	52.14	6.67	0.92	0.80	391	47	0.12	0.84
XJQ-5-1		1.70	2.92	0.32	1.23	0.27	0.06	0.22	0.03	0.18	0.03	0.08	0.01	0.08	0.01	1.43	47.52	7.14	0.93	1.01	56	48	0.86	1.35
ZC-5	Md1	30.86	56.13	5.72	21.23	4.17	0.79	3.50	0.50	2.78	0.53	1.41	0.23	1.66	0.25	20.11	37.94	129.76	0.95	0.91	71	62	0.87	1.12
ZC-7		3.42	7.77	1.04	4.45	1.08	0.21	0.91	0.14	0.82	0.15	0.38	0.06	0.41	0.06	7.35	48.97	20.90	0.83	0.93	67	264	3.94	0.95
XJG-15-2		10.82	19.89	1.97	6.51	1.23	0.22	1.02	0.14	0.76	0.15	0.42	0.07	0.51	0.08	8.29	55.29	43.78	0.87	0.89	63	74	1.17	1.12
XJQ-2-2	Md2	3.97	8.52	0.97	3.81	0.84	0.16	0.73	0.11	0.62	0.12	0.30	0.05	0.33	0.05	5.37	44.78	20.57	0.89	0.94	63	152	2.41	1.01
XJG-21-2		0.17	0.34	0.04	0.15	0.04	0.01	0.03	0.01	0.03	0.01	0.02	0.00	0.02	0.00	0.56	56.09	0.86	0.80	1.04	56	91	1.63	0.66
XJQ-3-2		1.50	2.54	0.27	1.06	0.25	0.04	0.20	0.03	0.15	0.03	0.07	0.01	0.07	0.01	1.93	64.28	6.23	0.96	0.77	55	122	2.22	1.33
XJG-19-1		0.72	1.57	0.21	0.85	0.21	0.04	0.17	0.02	0.13	0.02	0.06	0.01	0.06	0.01	1.32	66.15	4.10	0.78	0.99	48	110	2.29	1.24
ZC-16		0.39	0.75	0.09	0.35	0.08	0.01	0.07	0.01	0.07	0.01	0.04	0.01	0.04	0.01	0.58	57.63	1.95	0.79	0.82	115	89	0.77	0.77
ZC-31		4.10	7.47	0.81	2.85	0.60	0.13	0.46	0.06	0.34	0.07	0.19	0.03	0.19	0.03	3.21	45.79	17.33	0.85	1.06	55	122	2.22	1.31
HS1-4966	Md3	0.34	0.66	0.08	0.29	0.07	0.02	0.06	0.01	0.06	0.01	0.03	0.01	0.04	0.01	0.51	51.13	1.67	0.85	1.42	43	168	3.91	0.63
HS1-4971.3		0.31	0.63	0.08	0.30	0.07	0.03	0.06	0.01	0.05	0.01	0.03	0.00	0.03	0.01	0.62	61.74	1.62	0.81	2.22	19	315	16.58	0.88
ZC-23a		0.75	1.67	0.20	0.68	0.14	0.03	0.13	0.02	0.11	0.02	0.06	0.01	0.07	0.01	1.20	59.82	3.90	0.77	0.89	45	112	2.49	0.85
ZC-17		1.50	2.93	0.32	1.07	0.22	0.05	0.16	0.02	0.14	0.03	0.07	0.01	0.07	0.01	1.63	54.18	6.58	0.82	1.05	26	186	7.15	1.34
HS1-4977.9		0.31	0.61	0.07	0.25	0.06	0.02	0.06	0.01	0.05	0.01	0.03	0.01	0.04	0.01	0.69	69.46	1.52	0.83	1.25	29	191	6.59	0.55
HS1-4973.8		0.25	0.50	0.05	0.19	0.05	0.01	0.04	0.01	0.04	0.01	0.02	0.00	0.02	0.00	0.72	72.32	1.19	0.83	0.94	21	287	13.67	0.83
HS1-4982.6		0.53	1.02	0.13	0.44	0.11	0.03	0.09	0.01	0.08	0.02	0.05	0.01	0.05	0.01	1.53	76.54	2.58	0.75	1.36	32	157	4.91	0.77
ZC-13b	Cd	0.14	0.23	0.02	0.09	0.02	0.01	0.02	0.00	0.03	0.01	0.02	0.00	0.02	0.00	0.84	84.23	0.61	0.90	1.30	35	182	5.20	0.39
ZC-22b		0.38	0.66	0.07	0.27	0.07	0.03	0.05	0.01	0.05	0.01	0.03	0.00	0.03	0.01	0.71	70.91	1.68	0.85	2.17	28	226	8.07	0.79
ZC-23b		0.16	0.31	0.04	0.13	0.03	0.01	0.03	0.01	0.04	0.01	0.03	0.00	0.03	0.01	0.62	62.23	0.83	0.84	1.24	22	328	14.91	0.38

TABLE 4 | Fluid inclusion data of Middle Permian dolomites from the Western Sichuan Basin. (T_h—homogenization temperature; T_m—ice melting temperature).

Region	Sample	Lithology	T_h (°C)	T_m (°C)	Salinity (wt.%)
NW	HJL-5	Md2	89	−2.6	4.3
	HJL-7		92	−4.6	7.3
	HJL-8		94	−6.2	9.5
	HJL-7		99	−4.9	7.7
	K2 2446.9		100	−3.2	5.3
	HJL-17		100	−4.8	7.6
	K2-2416.3		103	−2.5	4.2
	K2-2446.9		106	−3.9	6.3
	HJL-5		109	−2.5	4.2
	K2-2416.3		109	−3.2	5.3
	HJL-16		112	−3.2	5.3
	K2-2432.4		117	−5.3	8.3
	K2-2432.4		118	−4.3	6.9
	K2-2416.3		118	−4.2	6.7
	K2-2432.4		119	−2.6	4.3
	HJL-16		125	−4.5	7.2
	HJL-11	Md3	107	−4.6	7.3
	HJL-9		110	−5.6	8.7
	HJL-9		118	−5.2	8.1
	HJL-9		124	−4.3	6.9
	HJL-13		125	−6.4	9.7
	HJL-11		127	−6.4	9.7
	HJL-14		130	−4.5	7.2
	HJL-11		122	−3.1	5.1
	HJL-9		135	−4.8	7.6
	HJL-14		138	−4.7	7.4
	HJL-10		139	−7.6	11.2
	HJL-13		136	−5.1	8.0
	HJL-10		142	−5.2	8.1
	HJL-14		144	−5.5	8.5
	HJL-4C	Cd	125	−5.5	8.5
NW	HJL-6C	Cd	129	−5.2	8.1
	HJL-4C		129	−6.4	9.7
	HJL-6C		131	−5.6	8.7
	HJL-4C		143	−6.1	9.3
	HJL-6C		135	−5.7	8.8
SW	ZC-16	Md2	96	−4.6	7.3
	ZC-16		102	−4.3	6.9
	ZC-16		115	−5.2	8.1
	ZC-31		121	−6.6	10.0
	ZC-31		99	−4.5	7.2
	ZC-31		107	−6.1	9.3
	ZC-31		113	−5.7	8.8
	XJQ-5-1		95	−4.4	7.0
	XJQ-5-1		88	−5.5	8.5
	XJQ-5-1		92	−5.7	8.8
	XJQ-5-1		82	−5.9	9.1
	HS1-4966	Md3	210	−11.3	15.3
	HS1-4966		203	−10.8	14.8
	HS1-4971.3		228	−14.5	18.2
	HS1-4971.3		221	−16.3	19.7
	HS1-4971.3		246	−13.4	17.3
	ZC-13b	Cd	220	−15.2	18.8
	ZC-13b		210	−8.4	12.2
	ZC-13b		193	−12.4	16.3
	ZC-13b		212	−18.9	21.6
	ZC-22b		187	−10.7	14.7
	ZC-22b		208	−12.1	16.1
	ZC-22b		204	−10.5	14.5
	ZC-22b		176	−9.3	13.2
	ZC-22b		243	−14.7	18.4
	ZC-22b		236	−15.2	18.8

$\delta^{18}O$ values are in the range of −7.4‰ to −6.5‰ (avg. −7.0‰), lower than those of Md1 and Md2. (**Table 1**; **Figure 9A**). Moreover, the Cd are with $\delta^{13}C$ values of 2.3‰–2.9‰ (avg. 2.7‰) and $\delta^{18}O$ values of −7.4‰ to −6.9‰ (avg. −7.1‰), which apparently overlap that of Md3 (**Table 1**; **Figure 5A**).

As for the southwestern Sichuan Basin, the $\delta^{13}C$ values of the limestone range from 3.4‰ to 4.6‰ (avg. 4.2‰) and the $\delta^{18}O$ values from −8.4‰ to −7.4‰ (avg. −7.8‰). The $\delta^{13}C$ values of Md1 range from 3.8‰ to 4.3‰ (avg. 4.1‰) and the $\delta^{18}O$ values from −8.6‰ to −5.2‰ (avg. −6.6‰). For Md2, $\delta^{13}C$ values are in the range of 3.4‰–4.7‰ (avg. 4.0‰) and the $\delta^{18}O$ values are in the range of −10.7‰ to −5.2‰ (avg. −7.3‰). Same as the northwestern Sichuan Basin, the $\delta^{13}C$ values of Md1 and Md2 are also of a similar range to that of limestone and Permian seawater. As for Md3, $\delta^{13}C$ values are 3.3‰–3.7‰ (avg. 3.5‰) and $\delta^{18}O$ values of −11.6‰ to −11‰ (avg. −11.3‰), of which the $\delta^{18}O$ values are much lower than that of Md1 and Md2. (**Table 1**; **Figure 9A**). In addition, Cd are with $\delta^{13}C$ values of 2.1‰–3.4‰ (avg. 2.9‰). And the $\delta^{18}O$ values of Cd range from −11.7‰ to −11.4‰ (avg. −11.6‰), which are the lowest all over the study area. Compared with the northwestern Sichuan Basin, the Md3 and CD of the southwestern Sichuan Basin possess the lower $\delta^{18}O$ values at almost 4‰ (**Figure 5B**; **Table 1**).

4.2.2 Radiogenic Sr Isotope Characteristics

In the northwestern Sichuan Basin, The $^{87}Sr/^{86}Sr$ ratios of the limestone range from 0.70707 to 0.70771 (avg. 0.70735), fitting with the approximate $^{87}Sr/^{86}Sr$ ratio range for Permian seawater (0.70680–0.70807; Veizer et al., 1999; Korte et al., 2006; Wang et al., 2019; Dong et al., 2020). The $^{87}Sr/^{86}Sr$ ratios of Md1 are from 0.70737 to 0.70785 (avg. 0.70763), which are similar to those of Md2 that range from 0.70727–0.70769 (avg. 0.70750). As for Md3, the $^{87}Sr/^{86}Sr$ ratios are 0.70738–0.70760 (avg. 0.70746). In addition, the $^{87}Sr/^{86}Sr$ ratios of Cd are from 0.70764–0.70779 (avg. 0.70771). In general, all the $^{87}Sr/^{86}Sr$ ratios of the four types of dolomites largely coincide with the range of coeval marine limestone (**Figure 6A**; **Table 1**).

In the southwestern Sichuan Basin, limestone had the same $^{87}Sr/^{86}Sr$ ratio (0.70682–0.70753, avg. 0.70715) as that of the Md1 (0.70732–0.070774, avg. 0.70753) and Md2 (0.70709–0.70801, avg. 0.70759), fitted with the $^{87}Sr/^{86}Sr$ ratio range for Permian seawater as well. However, the other dolomite types palpably possess a much higher $^{87}Sr/^{86}Sr$ ratio, which are Md3 (0.70870–0.71065, avg. 0.70972) and Cd (0.70958–0.71018, avg. 0.70988) (**Figure 6B**; **Table 1**).

4.2.3 Major and Trace Elements

In the northwestern Sichuan Basin, limestones are characterized by the lowest Mn concentrations (11–38 ppm and avg. 29 ppm) and highest Sr concentrations (289–313 ppm and avg. 303 ppm), with an average Mn/Sr ratio of 0.09. The Mn contents of Md1 are 49–62 ppm, with an average of 57 ppm, which are higher than those of limestone. On the contrary, the Sr contents of Md1 (76–105 ppm, avg. 86 ppm) are much lower than that of the limestones. The average Mn/Sr ratio of Md1 is 0.68. The Mn and

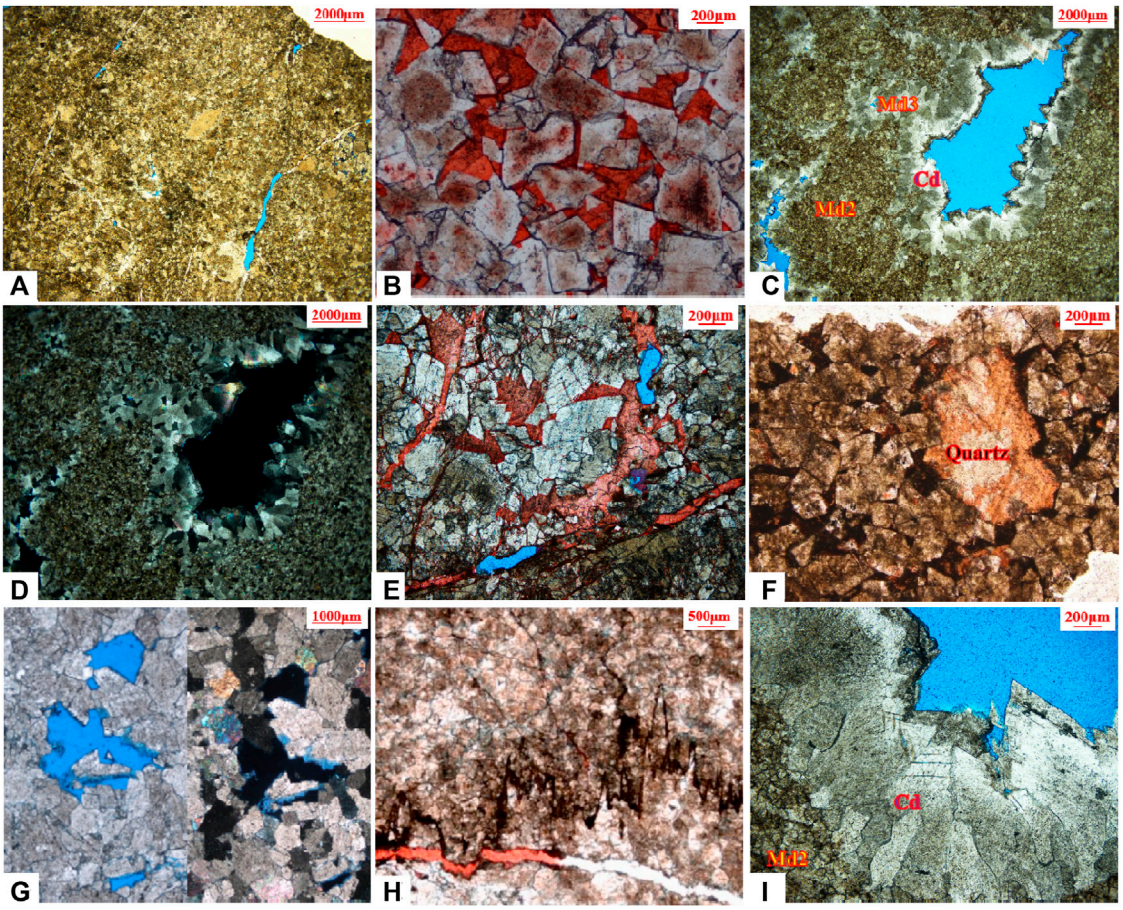

FIGURE 4 | Photos showing petrographical characteristics of different dolomites. **(A)** Very finely to finely crystalline Md1 with residual bioclastic structure and early-stage dissolution vugs and microfracture preserved (Sample ZC-5); **(B)** Idiomorphic-hypidiomorphic crystalline Md2 with cloudy-core and clear-rim (Sample K2-2406.5); **(C)** Cd filling in the dissolved pores close to the Md2 and Md3 (Sample XJG-3-2); **(D)** cross-polarized photomicrograph of **(C)**, Cd showing sharp undulatory extinction; **(E)** massive vugs and microfracture of Md3 are filled with calcite cements and bitumen (Sample HS1-4996); **(F)** Md3 with dissolved pores filled by authigenic quartz and calcite cements (Sample HS1-4977.9); **(G)** Md3 of coarsely to medium crystalline, nonplanar-a texture, and turbid crystals without clear rims, and the right half shows a sharp undulatory extinction under cross-polarized light (Sample HJL-10); **(H)** stylolites filled with bitumen-cut Md3 crystals and were later cut by microfracture filled with calcite cements (Sample HJL-13); **(I)** different-stage Cd filling in the hydraulic fracture close to the Md2 (Sample ZC-16).

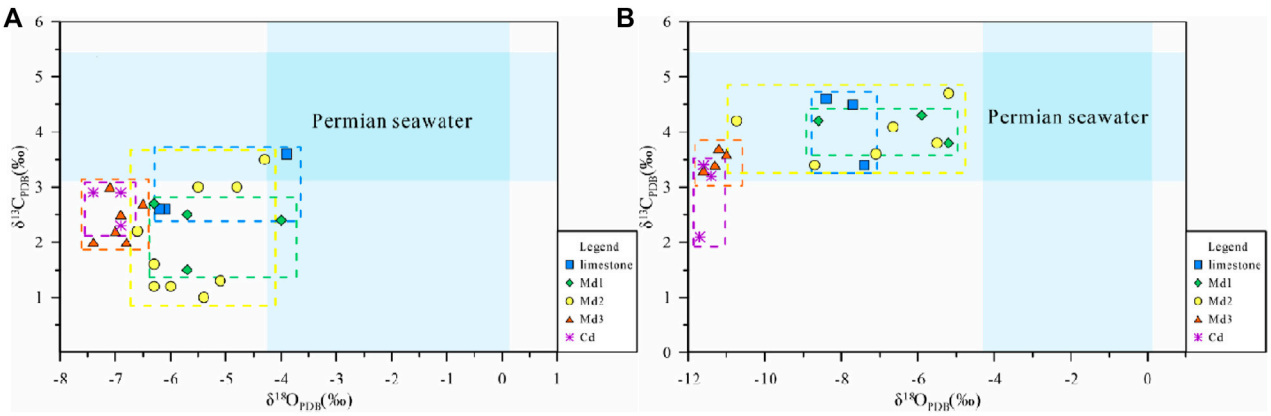

FIGURE 5 | Cross-plot of $\delta^{13}C$ versus $\delta^{18}O$ values of limestones and four types of dolomites in the Middle Permian compared to the Permian seawater (Buggisch et al., 2015). **(A)** Northwestern (NW) study area; **(B)** southwestern (SW) study area.

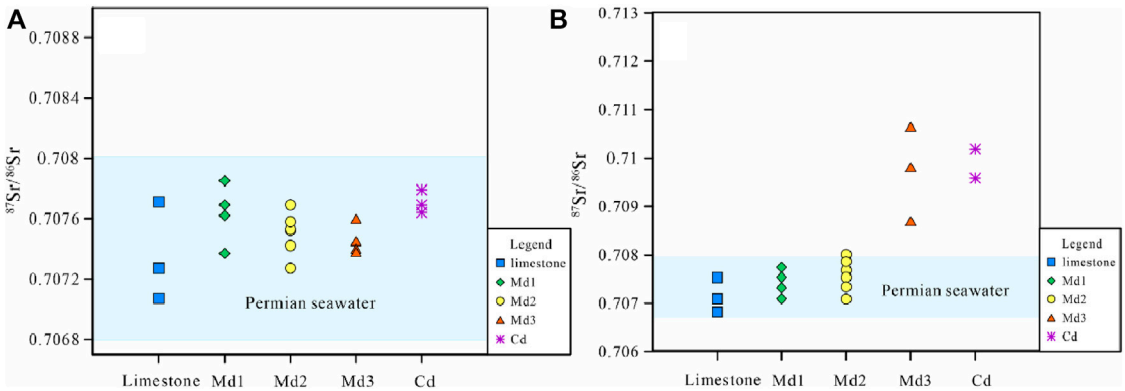

FIGURE 6 | $^{87}Sr/^{86}Sr$ ratios of limestones and four types of dolomites compared to the Permian seawater (0.70680–0.70807) (Veizer et al., 1999; Korte et al., 2006; Wang et al., 2019; Dong et al., 2020). **(A)** Northwestern (NW) study area; **(B)** southwestern (SW) study area.

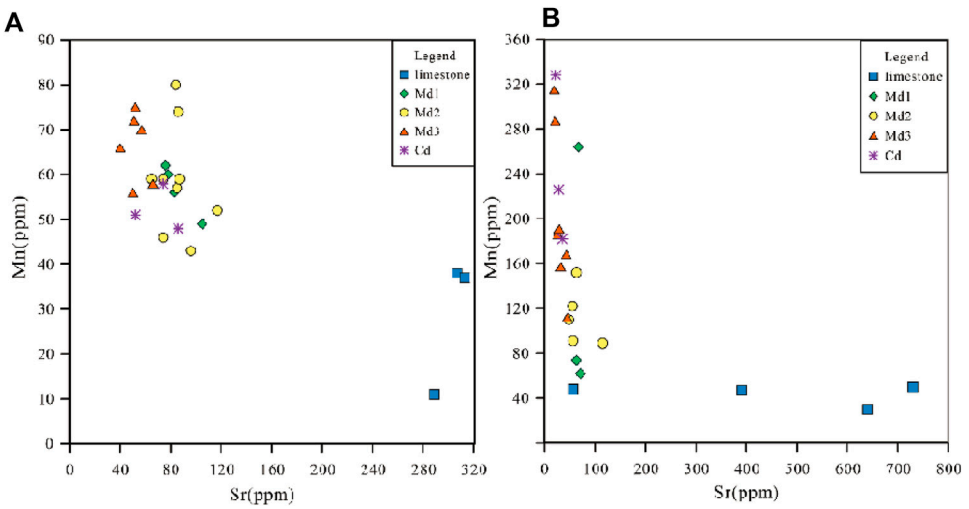

FIGURE 7 | Cross-plot of Sr versus Mn contents in limestones and four types of dolomites. **(A)** Northwestern (NW) study area; **(B)** southwestern (SW) study area.

Sr contents of Md2 are 43–80 ppm (avg. 59 ppm) and 65–117 ppm (avg. 85 ppm), respectively, with an average Mn/Sr ratio of 0.71, which are all similar to those of Md1. Md3 is slightly enriched in Mn (56–72 ppm, avg. 66 ppm) but reduced in Sr (40–66 ppm, avg. 53 ppm), with an average Mn/Sr ratio of 1.29. The Mn and Sr contents of Cd are 48–58 ppm (avg. 52 ppm) and 52–86 ppm (avg. 71 ppm), respectively, with the average Mn/Sr ratio of 0.77. In general, the average Mn concentration of Md1, Md2, and Md3 are relatively constant, while that of Cd are slightly lower. Compared with Md1 and Md2, the Md3 and Cd hold the lower Sr concentrations (**Figure 7A**; **Table 2**).

In the southwestern Sichuan Basin, Limestones also owns the lowest Mn concentrations (30–50 ppm, avg. 44 ppm) and highest Sr concentrations (56–730 ppm, avg. 454 ppm), with an average Mn/Sr ratio of 0.27. The Mn contents of Md1 (62–264 ppm, avg. 77 ppm) are higher than that of limestone while the Sr contents of Md1 (63–71 ppm, avg. 67 ppm) are apparently much lower. The average Mn/Sr ratio of Md1 is 2. The Mn and Sr contents of Md2 are 89–152 ppm (avg. 114 ppm) and 48–115 ppm (avg. 65 ppm), respectively, with an average Mn/Sr ratio of 1.92, which are similar to those of Md1. Md3 is obviously enriched in Mn (112–315 ppm, avg. 202 ppm) but reduced in Sr (19–45 ppm, avg. 31 ppm), with an average Mn/Sr ratio of 7.9. The Cd possess the highest Mn concentrations (182–328 ppm, avg. 245 ppm) and lowest Sr (22–35 ppm, avg. 28 ppm), with the average Mn/Sr ratio of 9.39. In general, the average Mn concentration of Md1 and Md2 are relatively constant, while that of Md3 and Cd are much higher. Compared with Md1 and Md2, the Md3 and Cd hold the low Sr concentrations (**Figure 7B**; **Table 2**).

In the northwestern Sichuan Basin, the total contents of REEs (ΣREE) in most dolomites and limestones do not vary substantially, with mostly low values of 1.41–4.92 ppm (avg. 2.55 ppm), except for a few limestone samples (K2-2456.5) and Md1 samples (HJL-1, HJL-2, and HJL-3), with higher

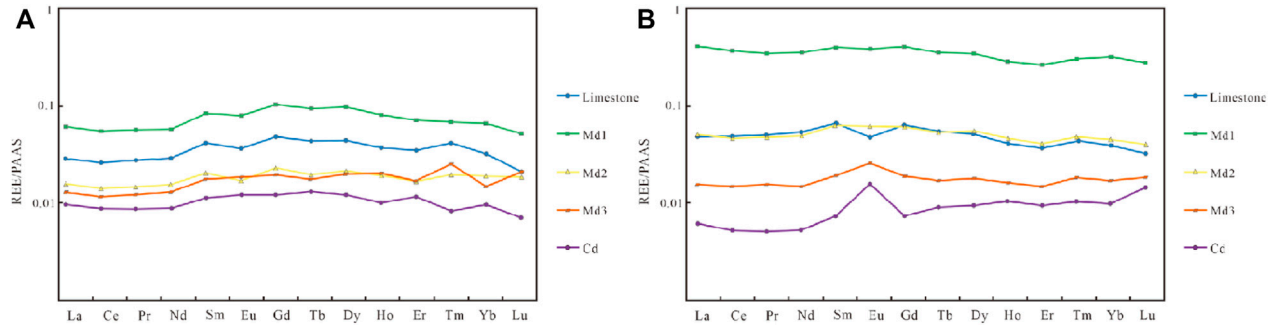

FIGURE 8 | Post-Archean Australian Shale (PAAS; Pourmand et al., 2012) normalized mean rare Earth element (REE) patterns of limestones and four types of dolomites. **(A)** Northwestern (NW) study area; **(B)** southwestern (SW) study area.

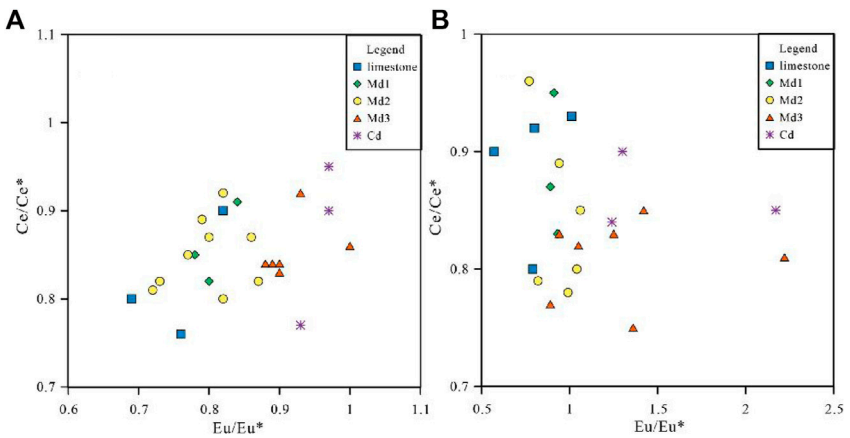

FIGURE 9 | Cross-plot of Eu/Eu* versus Ce/Ce* ratios in limestones and four types of dolomites. **(A)** Northwestern (NW) study area; **(B)** southwestern (SW) study area.

values of 10.46–15.38 (avg. 12.64 ppm). The PAAS-normalized REE of limestone and all types of dolomites consistently show flat REE patterns with negative Ce and Eu anomalies (**Figure 8A**). The Ce/Ce* values of all samples have small variations between 0.76 and 0.95 (avg. 0.85). However, the Eu/Eu* values of the different lithologies differ: those of limestone, Md1, and Md2 fall within a similar range from 0.69 to 0.87 (avg. 0.79), while those of Md3 and Cd are slightly higher (0.88–1.00, avg. 0.92, and 0.93–0.97, avg. 0.96, respectively) (**Figure 9A**; **Table 2**). The $(Nd/Yb)_{SN}$ ratios of Md1 and Md2 have a large range of 0.65–1.18 (avg. 0.85) while the Md3 and Cd have a narrower $(Nd/Yb)_{SN}$ range of 0.74–1.18 (avg. 0.91). In addition, the Y/Ho ratios of all samples are 42.81–78.64, with an average of 65.60 (**Table 2**).

In the southwestern Sichuan Basin, the ΣREE of Md1 is the highest (20.9–129.76 ppm, avg. 64.81 ppm), showing completely different mean REE patterns compared with that of limestone(3.49–17.86 ppm, avg. 8.79 ppm). The mean REE pattern of Md2 dolomite is similar to the limestone (**Figure 8B**), both showing relatively flat curves. The ΣREE of Md3 (1.19–6.58 ppm, avg. 2.72 ppm) and Cd (0.61–1.68 ppm, avg. 1.04 ppm) are both low, showing the similar mean REE patterns with positive Eu. The Ce/Ce* values of all samples also have small variations between 0.75 and 0.93 (avg. 0.85). The Eu/Eu* values of limestone, Md1, and Md2 fall within a similar range from 0.57 to 1.06 (avg. 0.89), while those of Md3 and Cd are higher (0.94–2.22, avg. 1.30, and 1.24–2.17, avg. 1.57, respectively) (**Figure 9B**; **Table 3**). The $(Nd/Yb)_{SN}$ of limestone (0.84–1.77, avg. 1.28) was higher than those of the other dolomites. The $(Nd/Yb)_{SN}$ of Md1 (0.95–1.12, avg. 1.06) and Md2 (0.66–1.33, avg. 1.05) are approximately the same, while the Md3 (0.55–1.34, avg. 0.84) and Cd (0.38–0.79, avg. 0.52) are lower. In addition, the Y/Ho ratios of all samples are 37.94–84.23, with an average of 57.89 (**Table 3**).

4.2.4 Fluid Inclusion Characteristics

A total of 36 fluid-inclusion samples in the northwestern Sichuan Basin were selected for measurement some of them were shown in the **Figure 10**. Fluid inclusions were not observed in the Md1. In the Md2, the fluid inclusion T_h values range from 89°C to 125°C (avg. 107°C), and the T_m

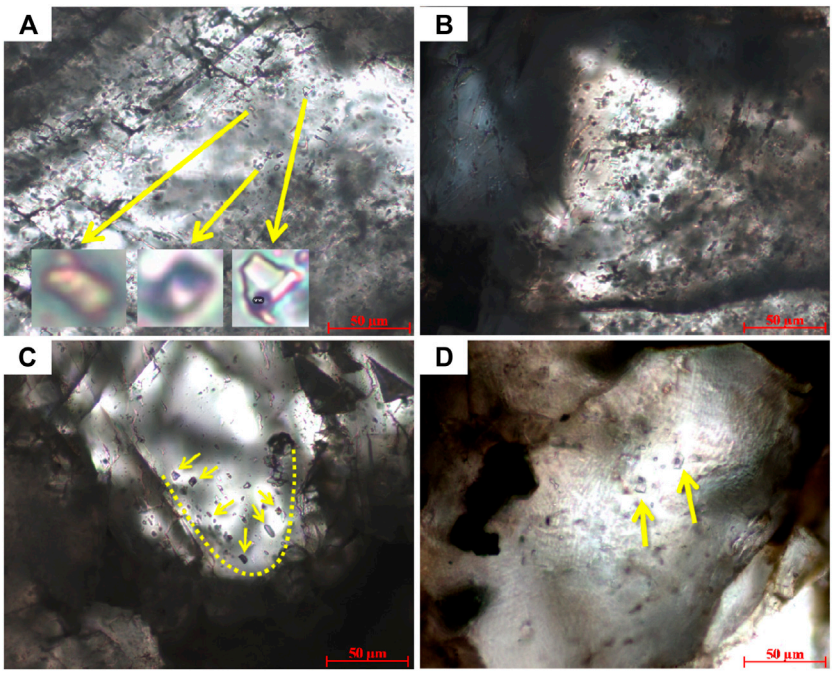

FIGURE 10 | Photomicrographs showing fluid inclusion petrography. **(A)** Liquid-dominated fluid inclusions were distributed along the edge of the crystal (Sample HS1-4966); **(B)** liquid-dominated fluid inclusions in random populations were distributed evenly in a crystal without special orientation (Sample K2-2432.4); **(C)** liquid-dominated fluid inclusions outlined the growth zone of Cd (Sample ZC-22b); **(D)** isolated fluid inclusions in the limpid Cd crystal (Sample HJL-6C).

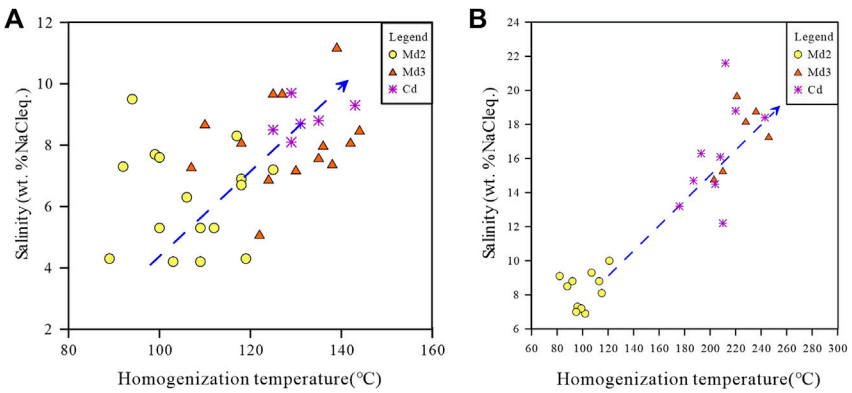

FIGURE 11 | Cross-plot of homogenization temperatures (T_h) versus salinity (calculated from final melting temperatures (T_m)) from fluid inclusions of Md2, Md3, and Cd. **(A)** Northwestern (NW) study area; **(B)** southwestern (SW) study area.

values range from −6.2°C to −2.6°C (avg. −3.9°C), with calculated salinities ranging from 4.2 wt% to 9.5 wt% (avg. 6.3 wt%). As for the Md3, the T_h values range from 107°C to 144°C (avg. 128°C), with corresponding salinities of 5.1 wt% to 11.2 wt% (avg. 8.1 wt%). The fluid inclusion T_h values of Cd are 125–143°C (avg. 132°C), with calculated salinities ranging from 8.1 wt% to 9.7 wt% (avg. 8.85 wt%) (**Figure 11A**; **Table 4**).

There are 26 fluid-inclusion samples selected in the southwestern Sichuan Basin. First in the Md2, the fluid inclusion T_h values and corresponding salinities are 88–121°C (avg. 101°C) and 6.9–10.0 wt% (avg. 8.3 wt%), respectively. Second, the fluid inclusion T_h values and calculated salinities of Md3 are 203–246°C (avg. 222°C) and 14.8–19.7 wt% (avg. 17.1 wt%), respectively. Lastly in the Cd, the T_h values range from 187 to 243°C (avg. 209°C), with the salinities of 12.2–21.6 wt% (avg. 16.5 wt%). In general, the T_h values and calculated salinities of Md3 and Cd are notably higher than that of the Md2, which are also far beyond that of samples in the northwestern Sichuan Basin (**Figure 11B**; **Table 4**).

5 DISCCUSSION

5.1 Estimation of the Fidelity of Geochemistry Data

The degrees of contamination of the samples by terrigenous clastic and diagenetic alteration were estimated to ensure the fidelity of the data before the result discussion. Terrigenous clastic contamination was assessed first. Trace elements of marine carbonate rocks are mainly affected by Fe and Mn oxides as well as terrigenous debris (such as shale) (Nothdurft et al., 2004). The Y/Ho ratios of global terrigenous sediments are relatively stabilized at a narrow range of 26–28, while that of marine sediments possess a larger range of 44–74 (Bau and Dulski, 1996; Webb and Kamber, 2000). The vast majority Y/Ho ratios of all samples in the northwest (42.81–78.64, avg. 65.60) and southwest (37.94–84.23, avg. 57.89) are within the range of marine sediments at the relatively high values, suggesting the minor influence of terrigenous input. Furthermore, the ΣREE of most samples in the study area is very low, which is also consistent with the low ΣREE feature of marine carbonates.

Second, the degree of diagenetic contamination was evaluated by the alteration of Sr concentrations and Mn/Sr values, for that the Sr is preferentially removed during the recrystallization of metastable carbonate rocks while the Mn is enriched in the formation of late Fe calcite cement (Kaufman, 1994; Korte et al., 2006). Generally, carbonates are considered to be without significant diagenetic alteration when Mn/Sr < 1.5 and $\delta^{18}O > -10‰$ (Fölling and Frimmel, 2002). The Mn/Sr ratios of all limestone samples in this study are <0.86, and the $\delta^{18}O$ values are > −8.6‰, which fell into the scope mentioned earlier indicating that there is no significant diagenetic alteration in the limestone samples of our study area, which can reflect ancient seawater composition. Meanwhile, the Mn/Sr ratios of majority of dolomite samples in the northwest are lower than 1.5, suggesting that they experienced minor diagenetic alteration (**Table 2**).

5.2 Deep Fluid Together With Seawater as Dolomitizing Fluid

5.2.1 Formation of Md1

In both northwest (NW) and southwest (SW) Sichuan Basin, the Md1 are characterized by very finely to finely crystalline and original structure preserved. The $\delta^{13}C$ values and $^{87}Sr/^{86}Sr$ ratio of Md1 are indistinguishable from that of the surrounding limestone and the Permian seawater (Korte et al., 2005; Mii et al., 2012; Buggisch et al., 2015; Wang et al., 2019; Dong et al., 2020), with the flat REE patterns almost in equilibrium with the surrounding limestone, indicating that the dolomitizing fluid was mainly coeval seawater. Moreover, the $\delta^{18}O$ values of Md1 are comparable to that of limestone, confirming that the penecontemporaneous seawater may be dominated in the dolomitization. However, affected by the abnormal heat carried by the deep fluid related to ELIP, the $\delta^{18}O$ values of Md1 are lower than those expected of normal Permian seawater dolomitizing fluids (Korte et al., 2005; Zhu et al., 2010). Furthermore, the $\delta^{18}O$ values in the SW are evidently lower than that in the NW, which may be caused by the decline of the impact of deep heat fluid of ELIP from SW to NW (**Figure 5**). In addition, whether in the SW or NW, the $\delta^{18}O$ values are evidently more negative than that of the typical evaporitic Permian dolomite (+0.2 to +7.4‰ V_{PDB}) (Peryt and Magaritz, 1990; Melim and Scholle, 2002) and it barely developed evaporative deposits, which suggest that the dolomitizing fluids are not from the evaporating process. In conclusion, the dolomitization fluid of Md1 is considered to be penecontemporaneous seawater without strong evaporation.

5.2.2 Formation of Md2

The stylolites are relatively developed in Md2, which clearly cut through the dolomite crystal (**Figure 4H**). Previous studies showed that the burial depth of the fully formed stylolites in the carbonate rock is about 500 m (Buxton and Sibley, 1981; Fabricius and Borre, 2007), so the formation environment of Md2 dolomite is considered a shallow burial condition (<500 m). Similar to Md1, the range of $\delta^{13}C$ values and $^{87}Sr/^{86}Sr$ ratios of Md2 overlap that of ambient limestone and the Permian seawater (**Figures 5**, **6**), which indicates that the dolomitizing fluids of Md2 are also derived from the Permian seawater. Moreover, Md1 and Md2 possess similar concentrations of Mn and Sr, which shows that Md2 was formed just a little bit later than Md1 (Budd, 1997). At the same time, the sign of the strong water-rock alteration by other fluids (e.g. hydrothermal fluids) that would have changed the REE composition (Qing and Mountjoy, 1994) is hard to be found in the study area. And it is obvious that the REE patterns, Ce anomalies, as well as Eu anomalies of Md2, are similitude to those of the limestones (**Figures 8**, **9**), which can be inferred that dolomitizing fluids were minimally affected by the external fluids. The $\delta^{18}O$ values of most samples in the Western Sichuan Basin are lower than host limestones and the Permian seawater, reflecting a higher formation temperature. The fluid inclusions in the Md2 support the heated seawater dolomitizing fluids as well. The T_h values measured in the fluid inclusion in the clear rims of Md2 (avg. 107.5°C in the NW and 101°C in the SW) are much higher than the maximum temperature of the shallow-burial 500 m strata (54°C, Dong et al., 2020). Meanwhile, the salinity calculated from T_m (avg. 6.3 wt% in the NW and 8.3 wt% in theSW) is higher than that of the Permian seawater (4.4 wt%), which may be related to the increased evaporation strength of seawater participating in thermal convection circulation due to the high temperature. Moreover, the evaporation in SW is stronger than in NW, thus showing slightly higher fluid inclusion salinity. Therefore, the dolomitization fluid of Md2 is considered to be originated from the Permian seawater in shallow burial strata, characterized by slightly higher temperature and salinity which may be caused by deep fluid related to ELIP.

5.2.3 Formation of Md3 and Cd

The genesis of dolomitization fluid of Md3 and Cd in the southwest (SW) differs from that of the northwest (NW) of the study area due to the different degrees of influence of deep fluids related to ELIP.

In the NW, the REE patterns, and ranges of $\delta^{13}C$ values of Md3 and Cd are basically consistent with those of other matrix dolomites and limestone, together with the uniform petrologic features of matrix dolomites, supporting that the Permian seawater donated in dolomitization. The Sr contents of Md3 and Cd are slightly lower than that of Md2, while the Mn contents are slightly higher (**Figure 7A**), implying that Md3 were formed later than Md2. The Mn contents are lower than that of the deep buried or hydrothermal dolomitizing fluid (Widodo and Laya, 2017; Zhao et al., 2018), which indicates there is no massive Mn injected by external fluids under the relatively closed and weakly oxidized shallow burial environment ((Budd, 1997; Veizer, 1978; Hou et al., 2016). Owing to the absorption of the radiogenic ^{87}Sr isotope, the hydrothermal dolomites are with high $^{87}Sr/^{86}Sr$ ratios (Montanez and Read, 1992; Davies and Smith, 2006; Wang et al., 2019; Dong et al., 2020). Apparently, the $^{87}Sr/^{86}Sr$ ratios of Md3 in the NW of our study area are much lower than those of hydrothermal dolomites, overlapping the range of $^{87}Sr/^{86}Sr$ ratios of Permian seawater (**Figure 6A**), excluding the hydrothermal origin of dolomitization fluid. However, the high-temperature deep fluid of ELIP still made an impact on the Md3 and Cd in NW. First of all, the crystals of Md 3 and Cd are characterized by nonplanar-a to saddle textures with more curved faces and wavy extinction, reflecting a disordered overgrowth of crystals rapidly at the relatively high temperature. Second, the $\delta^{18}O$, Eu/Eu*, T_h values and salinities calculated based on T_m of Md3 and Cd are obviously higher than those of Md2. However, the $\delta^{18}O$ values of Md3 and Cd in NW (avg. −6.99‰) are also much higher than that in SW (avg. −11.4‰) while the T_h values in NW (avg. 129°C) are much lower than that in SW (avg. 214°C), and the salinities are lower than that of the hydrothermal dolomite fluids as well (Davies and Smith, 2006). Thus, the low Mn contents, and similarity of $^{87}Sr/^{86}Sr$ ratios to the Permian seawater values, together with what was mentioned earlier, exclude the possibility of the large scale of hydrothermal dolomitizing fluids. There may be deep fluids of high temperatures and salinities associated with ELIP mixed with the dolomitizing fluids in some degrees. Generally, the Md3 and Cd in NW were formed at the period of shallow burial by seawater of relatively high-temperature mixed with deep fluids associated with ELIP to some degrees, and the crystals which were overgrown and recrystallized in the rapid circulation and diffusion of the dolomitizing fluids.

In the SW, the $\delta^{13}C$ values of Md3 and Cd dolomite cements are centralized and slightly lower than those of other types of dolomite (**Figure 5B**), indicating that other fluids may have provided an additional carbon source which reduced the $\delta^{13}C$ value. Mantle source carbon is usually light (−7‰ to −5‰), if discharged into diagenetic fluid and involved in the diagenesis of carbonate rocks, and the $\delta^{13}C$ value of primary rock will be reduced (Renne et al., 1995), but the reduction is less than that of the organic matter dilution (Liu et al., 2018). Thus, the slightly lower $\delta^{13}C$ value of some Md3 and Cd may be related to the mixing of deep fluid (magmatic hydrothermal) with mantle source characteristics provided by ELIP. The Sr contents of Md3 and Cd are slightly lower than that of Md2, also implying that Md3 were formed later than Md2. The Mn contents are evidently higher than that of the Md2 (**Figure 7B**), which shows the intensification of diagenesis and evolution of carbonate rocks and the input of Mn from external fluids. Additionally, the $^{87}Sr/^{86}Sr$ ratios of Md3 in the SW are much higher than that of Md3, Cd, and Permian seawater (**Figure 5B**). There are three following explanations: first, the diagenetic fluid was highly evaporated seawater and the evaporation caused the increase of ^{87}Sr in the fluid (Mountjoy et al., 1999; Nasir et al., 2008); second, a large amount of freshwater with high $^{87}Sr/^{86}Sr$ ratio was mixed in the diagenetic fluid (Compton et al., 2001; Meyers et al., 1997); third, the dolomitization fluid is the hydrothermal fluid or deep brine passing through the rich ^{87}Sr formation (Davies and Smith Jr, 2006; Jones and Jenkyns, 2001). However, in the sedimentary environment of the open carbonate platform, there barely developed evaporitic rock, and the $\delta^{18}O$ value of carbonate rocks was generally negative, excluding the existence of strong evaporation; meanwhile, there was no apparently covariant relationship between $\delta^{13}C$ and $\delta^{18}O$, so the mixed water as dolomitization fluid can also be excluded (Melim and Scholle, 2002). Therefore, the high $^{87}Sr/^{86}Sr$ ratio is considered to be related to the deep hydrothermal fluid associated with ELIP. Although the mantle source fluid has a very low $^{87}Sr/^{86}Sr$ ratio (<0.7045) (Hou et al., 2006), the $^{87}Sr/^{86}Sr$ ratio of dolomite formed or reconstructed by it could still be greatly increased when the hydrothermal fluid upwelled through the fault and passed through the underlying clastic rock stratum rich in ^{87}Sr due to tectonism (Davies and Smith Jr, 2006). Thus, it is inferred that the diagenetic fluid of Md3 and Cd was mixed with massive deep hydrothermal fluid. Moreover, the crystals of Md3 and Cd have apparently nonplanar-a to saddle textures with more curved faces and wavy extinction, reflecting a rapid formation under high temperature. The lower $\delta^{18}O$ values of Md3 and Cd in SW than other types of dolomites also support the high temperature. That the diagenetic fluid is acidic, high temperature hydrothermal fluid is also confirmed by positive Eu anomalies of Md3 and Cd dolomite (**Figures 8B**, **9B**) (Frimmel, 2009). What is more, the fluid inclusions provide more intuitive evidence of high temperature, with the T_h of inclusions in Md3 and Cd dolomite crystals from 176°C to 246°C (avg. 213°C), which are higher than that of Md2 (**Figure 11B**; **Table 4**). The salinity values of inclusions within Md3 and Cd are also much higher than that of Md2 and are comparable to the salinity of hydrothermal dolomite fluids calculated by Davies and Smith (2006). In conclusion, Md3 and Cd in SW are characterized by slightly lower $\delta^{13}C$, negative $\delta^{18}O$, low Sr content, high Mn content, high $^{87}Sr/^{86}Sr$ ratio, and high homogenization temperature and salinity, indicating a large amount of deep hydrothermal fluid taken part in the dolomitization.

5.3 Dolomitization Mechanism

Based on the aforementioned dolomitizing fluids, combined with the depositional settings, tectonic evolution, and burial history of the study area, we conclude different dolomitization mechanisms in SW and NW of the Middle Permian dolomite in Western Sichuan. The formation processes are as follows: (**Figure 12**).

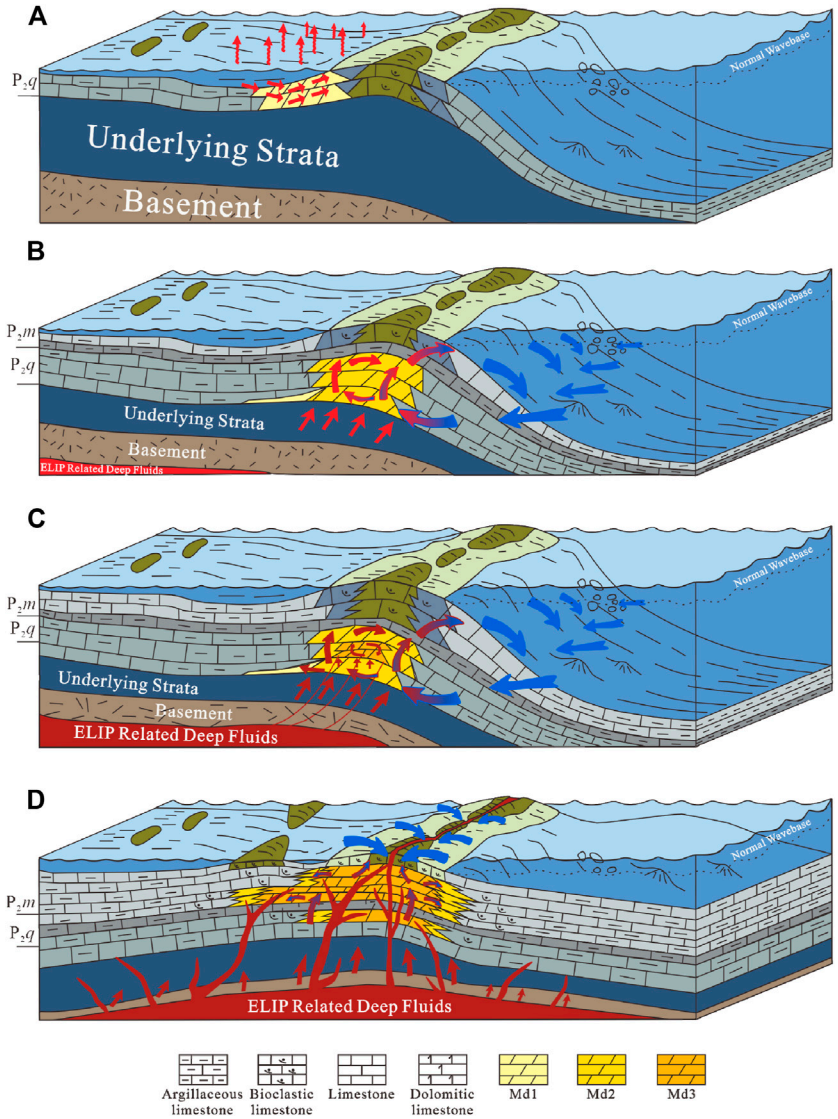

FIGURE 12 | Dolomitization pattern of the Middle Permian Formation in Western Sichuan Basin. **(A)** Seepage reflux dolomitization in the penecontemporaneous stage (Md1); **(B)** thermal convection dolomitization in the shallow burial stage (Md2); **(C)** high-temperature thermal convection dolomitization in shallow burial stage in NW (Md3 and Cd); **(D)** deep fluid participated in top and lateral open thermal convection at high temperature and structure-hydrothermal dolomitization in the shallow burial stage in SW (Md3 and Cd).

In both SW and NW of the study area, the diagenetic fluids of Md1 were all dominated by Permian seawater. The Md1 were in the relatively low energy and restricted environments (for example Lagoon, shoal edge, etc.), which could have a certain evaporation effect on the Permian seawater. However, the salinity levels of the Permian seawater might suggest to be insufficient which might be mesosaline or penesaline as evaporitic deposits have barely been found in the study area. Under the penecontemporaneous period, with the modification by BSR, the brackish and saturated seawater created conditions for the nucleation of dolomite, promoting the formation of "crystal seed" (crystal core), which laid a good foundation for the subsequent formation of Md2 (Warren, 2000; Choquette and Hiatt, 2008). It was followed by the process of extremely shallow burial. Affected by seawater density fluctuations and/or eustatic sea-level changes (Kaufman, 1994; Jones et al., 2003), the concentrated seawater continuously seeped and refluxed along the pores of the unconsolidated carbonate rocks of the high-energy shoal, leading to the overgrowth of the original dolomite seeds which further aggregated in Md1 (**Figure 12A**). Therefore, Md1 is considered to be seepage reflux dolomitization of slightly adjusted seawater at the peripheral of high energy shoals near the platform margin (Dong et al., 2020). Influenced by the geothermal warming effect brought by the deep fluid of ELIP, the evaporation was

more developed in the SW, and the seawater density fluctuation is accordingly more apparent, resulting in the more widely distributed Md1 in the SW than in the NW.

The dolomitization fluid of Md2 are still considered to be originated from the Permian seawater in shallow burial strata, characterized by slightly higher temperature and salinity which may be caused by the geothermal warming effect brought by deep fluid related to ELIP. The ELIP initiated at ~290 Ma and ended at ~240 Ma (Zhu et al., 2010). Just before and after the ELIP active period, under the "baking" of the abnormal heat from the deep fluid, a temperature difference between the warm pore water in the Middle Permian Formation of the heated platform and the cold deep ocean water was produced, which further brought about a density gradient, leading to a convection that upwards did the warm pore water flow while being drawn into the platform was the cold deep ocean water. Subsequently, the cold deep ocean water into the platform was heated, moved upwards or laterally afterward, discharging from under the confined layers, and finally, the forced thermal convection occurred (Kaufman, 1994; Sanford et al., 1998) (**Figure 12B**). The previous dolomite seeds in Md1 provide the basics for the dolomitization of Md2. In addition, the Mg^{2+} for the dolomitization was supplied constantly when the cold deep ocean water was ceaselessly poured into the platform. Moreover, as the kinetic rate constant and mineral saturation state were temperature-depended (Arvidson and Mackenzie, 1999; Wilson et al., 2001), the convective system would be strengthened while the geothermal temperature increased, leading to the dolomitization being intensified. Thus, the dolomitizing fluids of Md2 were mainly the heated seawater preserved in the porous infiltration system of strata, mixed with the cold seawater from the deep open ocean, and the Md2 were formed by thermal convection dolomitization. Furthermore, the SW was located in the middle zone of ELIP, of which the heat flow values reached 70~130 mW/m^2 at about 280~240 Ma, which was higher than that of NW in the outer zone of ELIP. Therefore, it was more conducive to the water-rock reaction of diagenetic fluid in the thermal convection system.

As for Md3 and Cd, there are some differences between the NW and SW. In the NW, seawater of relatively high-temperature dominated in the dolomitization process. The hot deep fluid might have intruded through the deep fractures with the activities of ELIP, providing a massive heat source below the Middle Permian Formation, further enhancing the convective flux (Wood and Hewett, 1982; Machel, 2004). With the accordingly promoted rate and degree of dolomitization, the Md3 of high temperature was thus formed. Similarly, as the high temperature promoted the dolomitization fluids recirculating in the highly permeable convection cell, the Cd was enabled to precipitate in pores, vugs, and fractures. In general, the Md3 and Cd of NW were mainly formed by high-temperature seawater-dominated thermal convection dolomitization (**Figure 12C**), while the deep fluid just provided the high temperature instead of the material source. Owing to the short eruption process of ELIP and the location of the outer zone of ELIP which is relatively far away, the abundance of Md3 and Cd are much less than that of Md2 in the NW; in the SW, a large amount of deep hydrothermal fluid mixed in the seawater and together participated in the dolomitization, instead of simply heated seawater. During the active period of ELIP, a large amount of deep fluid (magma and hydrothermal) surged along the basement fault zone and the associated syngenetic faults, passed through the medium-basic crystalline basement of the leaching basin, and many sets of underlying strata rich in clastic rocks, thus enriching a large number of Mg^{2+}. Thanks to the Md1 and Md2 formed by early dolomitization, the porosity and permeability of relevant formations were increased, so that the mixed dolomitizing fluid could continue to migrate laterally along with these high permeability formations and thus occurred structure-hydrothermal dolomitization at a high rate and degree (**Figure 12D**). Additionally, within the restricted platform, basement faults were active and relatively developed, with a high mixing degree of hydrothermal and seawater near the fault (Yapparova et al., 2017; Benjakul et al., 2020), which can form a fault-controlled top open thermal convection system in the intraplatform shoal and thus form a thermal convection dolomite with hydrothermal fluid properties. While in the platform margin zone, due to the upwelling of deep fluid through the faults, the temperature in the platform is further increased, and the dolomitized fluid mixed with hydrothermal and seawater can also form a higher temperature lateral open thermal convection cycle in the high permeability formation, so as to form dolomites with hydrothermal fluid properties. The early formed Md1 and Md2 were recrystallized through hydrothermal transformation to form Md3. Moreover, in the early formed karst caves, fractures, and hydraulic fracture structures caused by the hydrothermal intrusion, the hydrothermal fluid precipitated to form saddle Cd, and then the hydrothermal siliceous and other hydrothermal minerals were further filled in the pores and fractures. As the distance from the fault increased, the degree of deep hydrothermal fluid mixing into seawater was reduced, the temperature of the dolomitizing fluid gradually decreased, with Mg^{2+} gradually consumed, so that fewer Md1 and Md2 were recrystallized into Md3. Thus, the Md3 and Cd of SW were considered to be formed by structure-hydrothermal dolomitization and high-temperature thermal convection dolomitization of seawater mixed with hydrothermal.

5.4 The Effect of Deep Fluid on the Formation and Distribution of Dolomite

The distribution and volume of the dolomite body depend on the fluid composition, flow duration, and flow velocity of dolomitization. The fluid composition of dolomitization in the Middle Permian Formation in Western Sichuan is mainly seawater and a mixed fluid of seawater and deep fluid (hydrothermal). Therefore, when the dolomitization fluid is composed of deep fluid, the deep fluid activities related to ELIP can provide a sufficient material source (Mg^{2+} flux) for dolomitization. The final dolomitization may be the sum of

multiple dolomitization events, and the duration is regarded as the sum of multiple activity cycles.

The motive power of fluid flow is driven by fluid potential difference, of which the triggering factors mainly consist of terrain difference, fluid overpressure, rock deformation caused by tectonic action, and fluid density change caused by temperature or density difference. In the hydrothermal system, first, when the deep fluid (magma) invades, magma release occurs, which increases the fluid volume and forms overpressure (Chi and Xue, 2011). Second, strong tectonic movement activates a large number of basement faults, and the pressure is released intensively at the faults, which makes the hydrothermal fluid migrate upward along with the fault system (Oliver, 1986; Whitaker et al., 2004). In addition, the abnormal geothermal and the high temperature brought by the deep fluid lead to the decrease of fluid density, and the accompanying fluid density difference further leads to the significant fluid potential difference, which provides the strong migration power for the fluid. Therefore, in the ELIP, the overpressure, structural faults, and high temperature caused by deep fluid activities provided motive power for the migration of dolomitized fluid. Among them, the heating "baking" effect of deep fluid leads to the decrease of fluid density and faster flow rate in the formation pores inside the platform, and the difference of density is caused by the temperature difference between the heated pore fluid and the cold seawater outside the platform forms the thermal convection cycle of fluid. According to different geological conditions and backgrounds, under the comprehensive control of high permeability beach and basement faults, a lateral or top open thermal convection circulation system is formed in the Middle Permian Formation in Western Sichuan (Dong et al., 2020). Before and after the active period of ELIP, the permeable beach and basement fault zone are conducive to the transmission of heat and fluid, forming a seawater-dominated thermal convection unit; during the active period of ELIP, the deep fluid intruded along the basement fault zone on a large scale and provided higher heat, forming structure-hydrothermal dolomitization and the thermal convection unit of mixed fluid by seawater and hydrothermal.

In general, the deep fluid activities of ELIP provide not only the material source (Mg^{2+}) for the dolomitization process but also the migration motive power for the dolomitization fluid via overpressure, and tectonism, and high temperature. From the SW study area at the middle zone of ELIP to NW at the outer zone, the deep fluid activity decreases, the hydrothermal signal gradually weakens, the formation temperature of dolomite gradually decreases, and the distribution of dolomite is mostly controlled by high-permeability beach and basement faults, which further confirms that the Middle Permian dolomite in Western Sichuan is closely related to the deep fluid activity of ELIP.

6 CONCLUSION

(1) The petrological characteristics show that they are generally divided into four types of dolomite in the study area, which are matrix dolomite Md1 with very finely to finely crystalline size, Md2 with medium to finely crystalline size, and Md3 as well as cement dolomite (Cd) with coarsely to medium crystalline size.

(2) The dolomitizing fluids of Md1 and Md2 are mainly Permian seawater, which can be proved by similar $\delta^{13}C$ values, ranges of $^{87}Sr/^{86}Sr$ ratios, REE patterns, and Ce anomalies of dolomites compared to those of the ambient limestones. Among them, the Md1 is considered to be formed by seepage reflux dolomitization of slightly adjusted penecontemporaneous seawater at the peripheral of high energy shoals near the platform margin. What differs is that the dolomitizing fluid of Md2 performed to be with slightly higher T_h values and salinity caused by deep fluid activities of ELIP, which led to the thermal convection dolomitization when the heated seawater preserved in the porous infiltration system of strata contacted and circled with the cold seawater from the deep open ocean.

(3) Compared with Md2, the lower $\delta^{18}O$ and higher T_h values infer that Md3 and Cd were formed at a higher temperature influenced by the heat releasing of deep fluid from the ELIP. During the active eruption of the ELIP, the locally elevated temperature may have intensified the convective flux to form the higher-temperature thermal convective Md3 and Cd. In the NW of the study area, the dolomitizing fluid is dominated by heated seawater, while in the SW it was mixed with a large amount of deep fluid which was proved by lower $\delta^{13}C$ value and Sr contents, higher Mn contents, and $^{87}Sr/^{86}Sr$ ratios, positive Eu anomalies as well as much higher T_h and salinity values of inclusions, so that there was a superposition of structure-hydrothermal dolomitization compounded with the thermal convection dolomitization of seawater mixed with hydrothermal in SW.

(4) The deep fluid activities of ELIP provided not only the material source (Mg^{2+}) for the dolomitization process but also the migration motive power for the dolomitization fluid via overpressure, tectonism, and high temperature. From SW to NW, the deep fluid activity decreased, leading to the abundance reduction of Md3 and Cd, which were closely related to the hydrothermal solution. The deep fluid activities related to ELIP promoted the formation of dolomite, played a positive role in reservoir reconstruction, and provided more spaces for oil and gas accumulation.

DATA AVAILABILITY STATEMENT

The original contributions presented in the study are included in the article/Supplementary Material, further inquiries can be directed to the corresponding authors.

AUTHOR CONTRIBUTIONS

HH: Methodology, resources, investigation, and writing the original draft. HC: Validation, formal analysis, and visualization. FH: Editing, supervision, and data curation. SY: Conceptualization and data curation. AC: Supervision, reviewing,

and editing. All authors have read and agreed to the published version of the manuscript.

FUNDING

This research was funded by the Key Laboratory of Sedimentary Basins and Petroleum Resources, Ministry of Natural Resources of China (No. cdcgs2020004), and China Postdoctoral Science Foundation (2021M690485).

ACKNOWLEDGMENTS

The authors would like to thank all the reviewers and editors for the constructive help in manuscript revision.

REFERENCES

Adams, J. E., and Rhodes, M. L. (1960). Dolomitization by Seepage Reflexion. *AAPG Am. Assoc. Pet. Geol.) Bull.* 44, 1912–1920. doi:10.1306/0bda6263-16bd-11d7-8645000102c1865d

Arvidson, R. S., and Mackenzie, F. T. (1999). The Dolomite Problem; Control of Precipitation Kinetics by Temperature and Saturation State. *Am. J. Sci.* 299 (4), 257–288. doi:10.2475/ajs.299.4.257

Badiozamani, K. (1973). The Dorag Dolomitization Model–Application to the Middle Ordovician of Wisconsin. *J. Sediment. Res.* 43, 965–984.

Bau, M., and Dulski, P. (1996). Distribution of Yttrium and Rare-Earth Elements in the Penge and Kuruman Iron-Formations, Transvaal Supergroup, South Africa. *Precambrian Res.* 79, 37–55. doi:10.1016/0301-9268(95)00087-9

Benjakul, R., Hollis, C., Robertson, H. A., Sonnenthal, E. L., and Whitaker, F. F. (2020). Understanding Controls on Hydrothermal Dolomitisation: Insights from 3D Reactive Transport Modelling of Geothermal Convection. *Solid Earth Discuss.*, 1–35. doi:10.5194/se-11-2439-2020

Bissell, H. J., and Chilingar, G. V. (1967). Chapter 4 Classification of Sedimentary Carbonate Rocks. *Dev. Sedimentology* 9, 87–168. doi:10.1016/s0070-4571(08)71112-9

Budd, D. A. (1997). Cenozoic Dolomites of Carbonate Islands: Their Attributes and Origin. *Earth Sci. Rev.* 42 (1–2), 1–47. doi:10.1016/s0012-8252(96)00051-7

Buggisch, W., Krainer, K., Schaffhauser, M., Joachimski, M., and Korte, C. (2015). Late Carboniferous to Late Permian Carbon Isotope Stratigraphy: a New Record from Post-variscan Carbonates from the Southern Alps (Austria and Italy). *Palaeogeogr. Palaeoclimatol. Palaeoecol.* 433, 174–190. doi:10.1016/j.palaeo.2015.05.012

Buxton, T. M., and Sibley, D. F. (1981). Pressure Solution Features in a Shallow Buried Limestone. *J. Sediment. Res.* 51 (1), 19–26. doi:10.1306/212f7bf8-2b24-11d7-8648000102c1865d

Cai, C., Xie, Z., Worden, R. H., Hu, G., Wang, L., and He, H. (2004). Methane-dominated Thermochemical Sulphate Reduction in the Triassic Feixianguan Formation East Sichuan Basin, China: towards Prediction of Fatal H2S Concentrations. *Mar. Petroleum Geol.* 21, 1265–1279. doi:10.1016/j.marpetgeo.2004.09.003

Chen, X., Zhao, W., Liu, Y., Zhou, H., and Jiang, Q. (2013). Characteristics and Exploration Strategy of the Middle Permian Hydrothermal Dolomite in Southwestern Sichuan Basin. *Acta Pet. Sin.* 34, 460–466. (in Chinese with English abstract).

Chen, Z. (2009). Discussion on Gas Exploration of Middle Permian Qixia Formation. Sichuan Basin: Nat. *Gas. Geosci.* 20 (3), 325–334.

Chi, G. X., and Xue, C. J. (2011). Principle, Research Method and Application of Metallogenic Fluid Dynamics. *Earth Sci. Front.* 18 (05), 1–18.

Choquette, P. W., and Hiatt, E. E. (2008). Shallow-burial Dolomite Cement: a Major Component of Many Ancient Sucrosic Dolomites. *Sedimentology* 55 (2), 423–460. doi:10.1111/j.1365-3091.2007.00908.x

Compton, J., Harris, C., and Thompson, S. (2001). Pleistocene Dolomite from the Namibian Shelf: High 87Sr/86Sr and 18O Values Indicate an Evaporative, Mixed-Water Origin. *J. Sediment. Res.* 71 (5), 800–808. doi:10.1306/2dc40969-0e47-11d7-8643000102c1865d

Courtillot, V., Jaupart, C., Manighetti, I., Tapponnier, P., and Besse, J. (1999). On Causal Links between Flood Basalts and Continental Breakup. *Earth Planet Sci. Lett.* 166 (3–4), 177–195. doi:10.1016/s0012-821x(98)00282-9

Dai, J. X., Song, Y., Dai, C. S., Chen, A. F., Sun, M. L., Liao, Y. S., et al. (1995). *The Formation Conditions of Abiogenic Gas in Eastern China [M]*. Beijing: Science Press.

Davies, G. R., and Smith, L. B. (2006). Structurally Controlled Hydrothermal Dolomite Reservoir Facies: an Overview. *Bulletin* 90 (11), 1641–1690. doi:10.1306/05220605164

Dong, Y., Chen, H., Wang, J., Hou, M., Xu, S., Zhu, P., et al. (2020). Thermal Convection Dolomitization Induced by the Emeishan Large Igneous Province. *Mar. Petroleum Geol.* 116. doi:10.1016/j.marpetgeo.2020.104308

Du, L. J., Chen, J., Yang, R. D., Huang, Z. L., Zheng, L. L., Gao, J. B., et al. (2020). Mineralization of Volcanic Hydrothermal Deposits in the Middle-Late Permian Dachang Formation in Southwestern Guizhou [J]. *Geol. Rev.* 66 (02), 439–456.

Fabricius, I. L., and Borre, M. K. (2007). Stylolites, Porosity, Depositional Texture, and Silicates in Chalk Facies Sediments. Ontong Java Plateau ? Gorm and Tyra Fields, North Sea. *Sedimentology* 54 (1), 183–205. doi:10.1111/j.1365-3091.2006.00828.x

Feng, K., Xu, S., Chen, A., Ogg, J., Hou, M., Lin, L., et al. (2021). Middle Permian Dolomites of the SW Sichuan Basin and the Role of the Emeishan Large Igneous Province in Their Origin. *Mar. Petroleum Geol.* 128. doi:10.1016/j.marpetgeo.2021.104981

Fölling, P. G., and Frimmel, H. E. (2002). Chemostratigraphic Correlation of Carbonate Successions in the Gariep and Saldania Belts, Namibia and South Africa. *Basin Res.* 14 (1), 69–88.

Frimmel, H. E. (2009). Trace Element Distribution in Neoproterozoic Carbonates as Palaeoenvironmental Indicator. *Chem. Geol.* 258 (3-4), 338–353. doi:10.1016/j.chemgeo.2008.10.033

He, B., Xu, Y. G., Chung, S. L., Xiao, L., and Wang, Y. (2003). Sedimentary Evidence for a Rapid, Kilometer-Scale Crustal Doming Prior to the Eruption of the Emeishan Flood Basalts. *Earth Planet Sci. Lett.* 213 (3–4), 391–405. doi:10.1016/s0012-821x(03)00323-6

He, B., Xu, Y., Huang, X., Luo, Z., Shi, Y., Yang, Q., et al. (2007). Age and Duration of the Emeishan Flood Volcanism, SW China: Geochemistry and SHRIMP Zircon U–Pb Dating of Silicic Ignimbrites, Post-volcanic Xuanwei Formation and Clay Tuff at the Chaotian Section. *Earth Planet Sci. Lett.* 255 (3–4), 306–323. doi:10.1016/j.epsl.2006.12.021

Hou, M. C., Jiang, W. J., Xing, F. C., Xu, S. L., Liu, X. C., and Xiao, C. (2016). Origin of Dolomites in the Cambrian (Upper 3rd-Furongian) Formation, Southeastern Sichuan Basin, China. *Geofluids* 16 (5), 856–876. doi:10.1111/gfl.12193

Hou, Z., Lu, J., and Lin, S. (2006). Heterogeneity of a Plume axis: Bulk-Rock Geochemical Evidence from Picrites and Basalts in the Emei Large Igneous Province, Southwest China. *Int. Geol. Rev.* 48 (12), 1087–1112.

Hu, M., Hu, Z., Wei, G., Yang, W., and Liu, M. (2012). Sequence Lithofacies Paleogeography and Reservoir Prediction of the Maokou Formation in Sichuan Basin. *Pet. explor. Dev.* 39 (1), 45–55. doi:10.1016/s1876-3804(12)60014-7

Hu, W. X. (2016). Origin and Indicators of Deep Seated Fluids in Sedimentary Basins. *Bull. Mineralogy, Petrology Geochem.* 35 (5), 817–826.

Huang, H., Cawood, P. A., Hou, M.-C., Yang, J.-H., Ni, S.-J., Du, Y.-S., et al. (2016). Silicic Ash Beds Bracket Emeishan Large Igneous Province to. *Lithos* 264, 17–27. doi:10.1016/j.lithos.2016.08.013

Huang, H., He, D., Li, Y., and Wang, B. (2017). The Prototype and its Evolution of the Sichuan Sedimentary Basin and Adjacent Areas during Liangshan and Qixia Stages in Permian. *Acta Pet. Sin.* 4, 23.

Huang, S., Lv, J., Lan, Y., Huang, K., and Wang, C. (2011). The Main Texture of Dolomite of Middle Permian, Western Sichuan Basin: Concurrently on the Differences with Upper Permian-Triassic, Northeast Sichuan Basin. *Acta Pet. Sin.* 27 (8), 2253–2262.

Jiang, Q., Hu, S., Wang, Z., Wang, T., Li, Q., and Zhai, X. (2014). Genesis of Medium-Macrocrystalline Dolomite in the Middle Permian of Sichuan Basin. *Oil Gas. Geol.* 35 (4), 503–510.

Jiang, Z., Wang, X., Zeng, D., Lu, T., Wang, B., and Zhang, J. (2009). Constructive Diagenesis and Porosity Evolution in the Lower Permian Qixia Formation of Northwest Sichuan. *Chin. Geol.* 36 (1), 101–109.

Jin, Z., and Feng, Z. (1999). Origin of Dolostones of the Lower Permian in East Yunnan-West Sichuan: Dolomitization through Leaching of Basalts. *Acta Sedimentol. Sin.* 17 (3), 383–389.

Jin, Z. J., Yang, L., Zeng, J. H., and Zhang, L. P. (2002). Deep Fluid Activities and Their Effects on Generation of Hydrocarbon in Dongying Depression. *Petroleum Explor. Dev.* 29 (2), 42–44.

Jones, C. E., and Jenkyns, H. C. (2001). Seawater Strontium Isotopes, Oceanic Anoxic Events, and Seafloor Hydrothermal Activity in the Jurassic and Cretaceous. *Am. J. Sci.* 301 (2), 112–149. doi:10.2475/ajs.301.2.112

Jones, G. D., Smart, P. L., Whitaker, F. F., Rostron, B. J., and Machel, H. G. (2003). Numerical Modeling of Reflux Dolomitization in the Grosmont Platform Complex (Upper Devonian), Western Canada Sedimentary Basin. *Bulletin* 87 (8), 1273–1298. doi:10.1306/03260302007

Kaufman, J. (1994). Numerical Models of Fluid Flow in Carbonate Platforms. *J. Sediment. Res.* A64, 128–139.

Korte, C., Jasper, T., Kozur, H. W., and Veizer, J. (2006). $^{87}Sr/^{86}Sr$ Record of Permian Seawater. *Palaeogeogr. Palaeoclimatol. Palaeoecol.* 240 (1–2), 89–107. doi:10.1016/j.palaeo.2006.03.047

Korte, C., Jasper, T., Kozur, H. W., and Veizer, J. (2005). δ18O and δ13C of Permian Brachiopods: A Record of Seawater Evolution and Continental Glaciation. *Palaeogeogr. Palaeoclimatol. Palaeoecol.* 224 (4), 333–351. doi:10.1016/j.palaeo.2005.03.015

Liu, C., Du, Y., Jarochowska, E., Yan, J., Munnecke, A., and Lu, G. (2018). A Major Anomaly in the Carbon Cycle during the Late Cisuralian (Permian): Timing, Underlying Triggers and Implications. *Palaeogeogr. Palaeoclimatol. Palaeoecol.* 491, 112–122. doi:10.1016/j.palaeo.2017.11.061

Liu, C., Xie, Q., Wang, G., He, W., Song, Y., Tang, Y., et al. (2017). Rare Earth Element Characteristics of the Carboniferous Huanglong Formation Dolomites in Eastern Sichuan Basin, Southwest China: Implications for Origins of Dolomitizing and Diagenetic Fluids. *Mar. Petroleum Geol.* 81, 33–49. doi:10.1016/j.marpetgeo.2016.12.030

Liu, C. X., Li, T. G., and Liu, C. X. (2010). Deep Fluid Activity in Central Tarim Basin and its Heating Effects on Hydrocarbon Generation and Accumulation. *J. Jilin Univ. Earth Sci. Ed.* 40 (2), 279–285.

Liu, G. Y., Zhang, L. P., and Jin, Z. J. (2005). Primary Study on the Effects of Deep-Sourced Fluid's Movement on Hydrocarbon Migration. *Petroleum Geol. Exp.* 27 (3), 269–275.

Machel, H. G. (2004). "Concepts and Models of Dolomitization: a Critical Reappraisal," in *Geological Society, London, Special Publications*. Editors C. J. R. Braithwaite, G. Rizzi, and G. Darake (London: Geological Society, London, Special Publications), 235, 7–63. doi:10.1144/gsl.sp.2004.235.01.02

Mahoney, J. J., and Coffin, M. F. (1997). *Large Igneous Provinces: Continental, Oceanic, and Planetary Flood Volcanism*. American Geophysical Union.

Mattes, B. W., and Mountjoy, E. W. (1980). "Burial Dolomitization of the Upper Devonian Miette Buildup, Jasper National Park, Alberta," in *Concepts and Models of Dolomitization*. Editors D. H. Zengler, J. B. Dunham, and R. L. Ethington (Houston: SEPM Special Publication), 28, 259–297. doi:10.2110/pec.80.28.0259

Mei, Q., He, D., Gui, B., Li, Y ., Li, J., and Li, C. (2016). Multiple Rifting and its Evolution of Central Sichuan Basin in the Neoproterozoic-Paleozoic. *Nat. Gas. Geosci.* 27, 1427–1438.

Mei, Q., He, D., Wen, Z., Li, Y ., and Li, J. (2014). Geologic Structure and Tectonic Evolution of Leshan-Longnvsi Paleo-Uplift in Sichuan Basin, China. *Acta Pet. Sin.* 27, 1427–1438.

Melim, L. A., and Scholle, P. A. (2002). Dolomitization of the Capitan Formation Forereef Facies (Permian, West Texas and New Mexico): Seepage Reflux Revisited. *Sedimentology* 49 (6), 1207–1227. doi:10.1046/j.1365-3091.2002.00492.x

Meyers, W. J., Lu, F. H., and Zachariah, J. K. (1997). Dolomitization by Mixed Evaporative Brines and Freshwater, Upper Miocene Carbonates, Nijar, Spain. *J. Sediment. Res.* 67 (5), 898–912. doi:10.1306/d4268671-2b26-11d7-8648000102c1865d

Mii, H.-s., Shi, G. R., Cheng, C.-j., and Chen, Y.-y. (2012). Permian Gondwanaland Paleoenvironment Inferred from Carbon and Oxygen Isotope Records of Brachiopod Fossils from Sydney Basin, Southeast Australia. *Chem. Geol.* 291, 87–103. doi:10.1016/j.chemgeo.2011.10.002

Montanez, I. P., and Read, J. F. (1992). Fluid-rock Interaction History during Stabilization of Early Dolomites, Upper Knox Group (Lower Ordovician), US Appalachians. *J. Sediment. Res.* 62 (5), 753–778. doi:10.1306/d42679d3-2b26-11d7-8648000102c1865d

Mountjoy, E. W., Machel, H. G., Green, D., Duggan, J., and Williams-Jones, A. E. (1999). Devonian Matrix Dolomites and Deep Burial Carbonate Cements: a Comparison between the Rimbey-Meadowbrook Reeftrend and the Deep Basin of West-Central Alberta. *Bull. Can. Petroleum Geol.* 47 (4), 487–509.

Nasir, S., Al-Saad, H., Alsayigh, A., and Weidlich, O. (2008). Geology and Petrology of the Hormuz Dolomite, Infra-cambrian: Implications for the Formation of the Salt-Cored Halul and Shraouh Islands, Offshore, State of Qatar. *J. Asian Earth Sci.* 33 (5-6), 353–365. doi:10.1016/j.jseaes.2008.02.003

Nothdurft, L. D., Webb, G. E., and Kamber, B. S. (2004). Rare Earth Element Geochemistry of Late Devonian Reefal Carbonates, Canning Basin, Western Australia: Confirmation of a Seawater REE Proxy in Ancient Limestones. *Geochimica Cosmochimica Acta* 68, 263–283. doi:10.1016/s0016-7037(03)00422-8

Oliver, J. (1986). Fluids Expelled Tectonically from Orogenic Belts: Their Role in Hydrocarbon Migration and Other Geologic Phenomena. *Geol* 14 (2), 99–102. doi:10.1130/0091-7613(1986)14<99:fetfob>2.0.co;2

Peryt, T. M., and Magaritz, M. (1990). Genesis of Evaporite-Associated Platform Dolomites: Case Study of the Main Dolomite (Zechstein, Upper Permian), Leba Elevation, Northern Poland. *Sedimentology* 37 (4), 745–761. doi:10.1111/j.1365-3091.1990.tb00632.x

Pourmand, A., Dauphas, N., and Ireland, T. J. (2012). A Novel Extraction Chromatography and MC-ICP-MS Technique for Rapid Analysis of REE, Sc and Y: Revising CI-Chondrite and Post-Archean Australian Shale (PAAS) Abundances. *Chem. Geol.* 291, 38–54. doi:10.1016/j.chemgeo.2011.08.011

Qing, H., and Mountjoy, E. W. (1994). Formation of Coarsely Crystalline, Hydrothermal Dolomite Reservoirs in the Presqu'ile Barrier, Western Canada Sedimentary Basin. *AAPG Bull.* 78 (1), 55–77. doi:10.1306/bdff9014-1718-11d7-8645000102c1865d

Ramkumar, M., Siddiqui, N. A., Mathew, M., Sautter, B., Hui, P. X., Nagarajan, R., et al. (2019). Structural Controls on Polyphase Hydrothermal Dolomitization in the Kinta Valley, Malaysia: Paragenesis and Regional Tectono-Magmatism. *J. Asian Earth Sci.* 174, 364–380. doi:10.1016/j.jseaes.2019.02.004

Renne, P. R., Black, M. T., Zichao, Z., Richards, M. A., and Basu, A. R. (1995). Synchrony and Causal Relations between Permian-Triassic Boundary Crises and Siberian Flood Volcanism. *Science* 269 (5229), 1413–1416. doi:10.1126/science.269.5229.1413

Richardson, N. J., Densmore, A. L., Seward, D., Fowler, A., Wipf, M., Ellis, M. A., et al. (2008). Extraordinary Denudation in the Sichuan Basin: Insights from Low-Temperature Thermochronology Adjacent to the Eastern Margin of the Tibetan Plateau. *J. Geophys. Res. Solid Earth* 113 (B4). doi:10.1029/2006jb004739

Saitoh, M., Isozaki, Y., Ueno, Y., Yoshida, N., Yao, J., and Ji, Z. (2013). Middle-Upper Permian Carbon Isotope Stratigraphy at Chaotian, South China: Pre-extinction Multiple Upwelling of Oxygen-Depleted Water onto Continental Shelf. *J. Asian Earth Sci.* 67-68, 51–62. doi:10.1016/j.jseaes.2013.02.009

Sanford, W. E., Whitaker, F. F., Smart, P. L., and Jones, G. (1998). Numerical Analysis of Seawater Circulation in Carbonate Platforms; I, Geothermal Convection. *Am. J. Sci.* 298 (10), 801–828. doi:10.2475/ajs.298.10.801

Scotese, C. R., and Schettino, A. (2017). *Late Permian-Early Jurassic Paleogeography of Western Tethys and the World, Permo-Triassic Salt Provinces of Europe, North Africa and the Atlantic Margins*. Elsevier, 57–95. doi:10.1016/b978-0-12-809417-4.00004-5

Shellnutt, J. G., Denyszyn, S. W., and Mundil, R. (2012). Precise Age Determination of Mafic and Felsic Intrusive Rocks from the Permian Emeishan Large Igneous Province (SW China). *Gondwana Res.* 22 (1), 118–126. doi:10.1016/j.gr.2011.10.009

Simms, M. (1984). Dolomitization by Ground Water-Flow Systems in Carbonate Platforms. *AAPG Am. Assoc. Pet. Geol.) Bull.* 68, 1219–1220. doi:10.1306/ad46189a-16f7-11d7-8645000102c1865d

Song, X. Y., Qi, H. W., Robinson, P. T., Zhou, M. F., Cao, Z. M., and Chen, L. M. (2008). Melting of the Subcontinental Lithospheric Mantle by the Emeishan

Mantle Plume: Evidence from the Basal Alkaline Basalts in Dongchuan, Yunnan, Southwestern China. *Lithos* 100 (1-4), 93–111. doi:10.1016/j.lithos.2007.06.023

Steele-MacInnis, M., Bodnar, R. J., and Naden, J. (2011). Numerical Model to Determine the Composition of H2O-NaCl-CaCl2 Fluid Inclusions Based on Microthermometric and Microanalytical Data. *Geochimica Cosmochimica Acta* 75, 21–40. doi:10.1016/j.gca.2010.10.002

Sun, Y. D., Lai, X. L., Wignall, P. B., Widdowson, M., Ali, J. R., Jiang, H. S., et al. (2010). Dating the Onset and Nature of the Middle Permian Emeishan Large Igneous Province Eruptions in SW China Using Conodont Biostratigraphy and its Bearing on Mantle Plume Uplift Models. *Lithos* 119 (1-2), 20–33. doi:10.1016/j.lithos.2010.05.012

Tian, J., Lin, X., Zhang, X., Peng, S., and Yang, C. (2014). Multi-general Mechanism and Superposition Effect of the Shoal Dolomite in Qixia Formation of Middle Permian in Sichuan Basin. *Acta Pet. Sin.* 30 (3), 679–686.

Veizer, J., Ala, D., Azmy, K., Bruckschen, P., Buhl, D., Bruhn, F., et al. (1999). $^{87}Sr/^{86}Sr$, $\delta^{13}C$ and $\delta^{18}O$ Evolution of Phanerozoic Seawater. *Chem. Geol.* 161 (1–3), 59–88. doi:10.1016/s0009-2541(99)00081-9

Veizer, J. (1978). Secular Variations in the Composition of Sedimentary Carbonate Rocks, II. Fe, Mn, Ca, Mg, Si and Minor Constituents. *Precambrian Res.* 6 (3–4), 381–413. doi:10.1016/0301-9268(78)90024-4

Wang, J., Jacobson, A. D., Zhang, H., Ramezani, J., Sageman, B. B., Hurtgen, M. T., et al. (2019). Coupled δ44/40Ca, δ88/86Sr, and 87Sr/86Sr Geochemistry across the End-Permian Mass Extinction Event. *Geochimica Cosmochimica Acta* 262, 143–165. doi:10.1016/j.gca.2019.07.035

Warren, J. (2000). Dolomite: Occurrence, Evolution and Economically Important Associations. *Earth-Science Rev.* 52 (1-3), 1–81. doi:10.1016/s0012-8252(00)00022-2

Webb, G. E., and Kamber, B. S. (2000). Rare Earth Elements in Holocene Reefal Microbialites: a New Shallow Seawater Proxy. *Geochimica Cosmochimica Acta* 64, 1557–1565. doi:10.1016/s0016-7037(99)00400-7

Wei, G., Du, J., Xu, C., Zou, C., Yang, W., Shen, P., et al. (2016). Characteristics and Accumulation Mode of Large-Scale Sinian-Cambrian Gas Reservoirs in the Gaoshiti-Moxi Region, Sichuan Basin. *Petroleum Res.* 1, 164–177. doi:10.1016/s2096-2495(17)30040-6

Wei, G., Yang, W., Zhu, Y., Jin, H., Li, Y., Shi, Z., et al. (2010). Depositional System of the Middle Permian Qixia Formation in the Western Sichuan Basin. *Oil Gas. Geol.* 31, 442–448. (in Chinese with English abstract).

Whitaker, F. F., Smart, P. L., and Jones, G. D. (2004). Dolomitization: from Conceptual to Numerical Models. *Geol. Soc. Lond. Spec. Publ.* 235 (1), 99–139. doi:10.1144/gsl.sp.2004.235.01.05

Widodo, R. W., and Laya, J. C. (2017). Controls on Diagenesis and Dolomitization of Peritidal Facies, Early Cretaceous Lower Edwards Group, Central Texas, USA. *Facies* 63 (4), 23. doi:10.1007/s10347-017-0503-2

Wilson, A. M., Sanford, W., Whitaker, F., and Smart, P. (2001). Spatial Patterns of Diagenesis during Geothermal Circulation in Carbonate Platforms. *Am. J. Sci.* 301 (8), 727–752. doi:10.2475/ajs.301.8.727

Wood, J. R., and Hewett, T. A. (1982). Fluid Convection and Mass Transfer in Porous Sandstones-A Theoretical Model. *Geochimica Cosmochimica Acta* 46 (10), 1707–1713. doi:10.1016/0016-7037(82)90111-9

Xia, L., Cao, J., Stüeken, E. E., Zhi, D., Wang, T., and Li, W. (2020). Unsynchronized Evolution of Salinity and pH of a Permian Alkaline Lake Influenced by Hydrothermal Fluids: a Multi-Proxy Geochemical Study. *Chem. Geol.*, 119581. doi:10.1016/j.chemgeo.2020.119581

Xiao, D., Zhang, B., Tan, X., Liu, H., Xie, J., Wang, L., et al. (2018). Discovery of a Shoal-Controlled Karst Dolomite Reservoir in the Middle Permian Qixia Formation, Northwestern Sichuan Basin, Southwest China. *Energy Explor. Exploitation* 36 (4), 686–704. doi:10.1177/0144598717733592

Xu, Y.-G., He, B., Chung, S.-L., Menzies, M. A., and Frey, F. A. (2004). Geologic, Geochemical, and Geophysical Consequences of Plume Involvement in the Emeishan Flood-Basalt Province. *Geol* 32 (10), 917–920. doi:10.1130/g20602.1

Xu, Y.-G., Luo, Z.-Y., Huang, X.-L., He, B., Xiao, L., Xie, L.-W., et al. (2008). Zircon U-Pb and Hf Isotope Constraints on Crustal Melting Associated with the Emeishan Mantle Plume. *Geochimica Cosmochimica Acta* 72 (13), 3084~3104–3104. doi:10.1016/j.gca.2008.04.019

Yapparova, A., Gabellone, T., Whitaker, F., Kulik, D. A., and Matthäi, S. K. (2017). Reactive Transport Modelling of Hydrothermal Dolomitisation Using the CSMP++GEM Coupled Code: Effects of Temperature and Geological Heterogeneity. *Chem. Geol.* 466, 562–574. doi:10.1016/j.chemgeo.2017.07.005

Zeng, J. H. (2000). Thermal Fluid Activities and Their Effects on Waterrock Interaction in Dongying Sag. *Earth Sci. J. China Univ. Geosciences* 25 (2), 133–142.

Zhang, B., Xie, J., Hong, Y., Wang, Y., Yang, X., and Pei, S. (2018). Characteristics and Exploration Direction of the Middle Permian Carbonate Reservoirs in the Longmenshan Mountain Areas, Western Sichuan Basin. *Nat. Gas. Ind.* 38 (2), 33–42.

Zhang, L., Zhang, X. T., Liu, Y. M., Han, R., and Wei, G. C. (2021). Evidence of Deep Fluid and its Influence on Gas Reservoiring in Bohai Sea: Case Study of QHD29-2/2E Oilfield. *Nat. Gas. Geosci.* 32 (5), 633–644.

Zhang, M. J., Wang, X. B., and Li, L. W. (2000). Composition of Mantle Fluid. *Earth Sci. Front.* 7 (2), 401–412.

Zhao, Y.-Y., Zhao, M.-Y., and Li, S.-Z. (2018). Evidences of Hydrothermal Fluids Recorded in Microfacies of the Ediacaran Cap Dolostone: Geochemical Implications in South China. *Precambrian Res.* 306, 1–21. doi:10.1016/j.precamres.2017.12.028

Zhao, Z., Zhou, H., Chen, X., Liu, Y., Zhang, Y., and Liu, Y. e. (2012). Sequence Lithofacies Paleogeography and Favorable Exploration Zones of the Permian in Sichuan Basin and Adjacent Areas. *Acta Pet. Sin.* 33 (S2), 35–51.

Zheng, H. F., Ma, Y. S., Chi, G. X., Qing, H. R., Liu, B., Zhang, X. F., et al. (2019). Stratigraphic and Structural Control on Hydrothermal Dolomitization in the Middle Permian Carbonates, Southwestern Sichuan Basin (China). *Minerals* 9 (32), 1–31. doi:10.3390/min9010032

Zhou, H., Wang, Q., Zhao, J., Zheng, L., Guan, H., Feng, Y., et al. (2008). Rare Earth Elements and Yttrium in a Stalagmite from Central China and Potential Paleoclimatic Implications. *Palaeogeogr. Palaeoclimatol. Palaeoecol.* 270, 128–138. doi:10.1016/j.palaeo.2008.09.001

Zhou, J., Yao, G., Yang, G., Gu, M., Yao, Q., Jiang, Q., et al. (2016). Lithofacies Paleogeography and Favorable Gas Exploration Zones of Qixia and Maokou Formations in the Sichuan Basin. *Nat. Gas. Ind.* 36, 8–15.

Zhu, B., Guo, Z., Zhang, S., Ukstins, I., Du, W., and Liu, R. (2019). What Triggered the Early-Stage Eruption of the Emeishan Large Igneous Province? *Bulletin* 131 (11–12), 1837–1856. doi:10.1130/b35030.1

Zhu, C., Xu, M., Yuan, Y., Zhao, Y., Shan, J., He, Z., et al. (2010). Palaeogeothermal Response and Record of the Effusing of Emeishan Basalts in the Sichuan Basin. *Chin. Sci. Bull.* 55, 949–956. doi:10.1007/s11434-009-0490-y

Conflict of Interest: The authors declare that the research was conducted in the absence of any commercial or financial relationships that could be construed as a potential conflict of interest.

Publisher's Note: All claims expressed in this article are solely those of the authors and do not necessarily represent those of their affiliated organizations, or those of the publisher, the editors, and the reviewers. Any product that may be evaluated in this article, or claim that may be made by its manufacturer, is not guaranteed or endorsed by the publisher.